UNIVERSITÀ DEGLI STUDI DI PADOVA

DIPARTIMENTO DI TECNICA E GESTIONE DEI SISTEMI INDUSTRIALI
CORSO DI LAUREA MAGISTRALE IN
INGEGNERIA DELL'INNOVAZIONE DEL PRODOTTO

TESI DI LAUREA MAGISTRALE IN
INGEGNERIA DELL'INNOVAZIONE DEL PRODOTTO

MICROSTRUCTURAL TRANSFORMATIONS OF DIFFERENT DUPLEX STAINLESS STEELS IN ADVANCED TECHNOLOGICAL PROCESSES

Relatore: Prof.ssa Irene Calliari
Correlatore: Prof. Istvan Mészàros

Laureando: Luca Brazzalotto

ANNO ACCADEMICO 2016/2017

ABSTRACT

Duplex stainless steels (DSSs) are a particular category of stainless steels, which are employed in all the kinds of applications where both high strength and excellent corrosion resistance are required. This favourable combination of properties is provided by their biphasic microstructure, consisting of ferrite and austenite in almost equal volume fractions. Nevertheless, these materials may suffer from several microstructural transformations if they undergo heat treatments or welding processes. These transformations modify the balanced phase ratio, compromising the corrosion and mechanical properties of the material. In this thesis the microstructural stability as a consequence of heat treatments and welding processes has been investigated for different DSSs. During this work, three main research activities have been conducted.

Firstly, the decomposition of the ferritic phase has been studied in isothermally aged SAF 2507 SDSS using different examination methods. Samples have been heat treated at two different temperatures, T=800°C and T=850°C. Results show that: the decomposition of ferrite increases with increasing of aging time. T=850°C is the most critical temperature for ferrite decomposition, with an incubation time of 5 minutes for σ-phase precipitation. The σ-phase started to precipitate at the ferrite/austenite junction, and then grew towards ferritic grains. The precipitation of σ-phase brought to an increase in material hardness.

Secondly, the effects of laser beam welding on SAF 2507 SDSS previously cold rolled have been investigated. Samples have been cold rolled at different grades of reduction (ε =10%,20%,30%,40%,50%,60%) and then welded using the Nd:YAG laser welding process. OM analysis, Eddy current tests, Microhardness tests and corrosion tests have been performed on the welded samples to analyse the microstructure, ferrite content, hardness and corrosion resistance. Results show that: laser welded joints had a strongly unbalanced microstructure, mostly consisting of ferritic phase (~64%). Ferrite content decreased with increasing distances from the middle of the joint. The HAZ was almost undetectable and no defects or secondary phases have been observed. Both the hardness and the corrosion rate of the joints increased. Previous cold rolled deformation had no effects in microstructure, hardness or corrosion resistance of the joints, but induced an increase of hardness in the base material.

Finally, the effect of backing gas composition on lean duplex grades LDX 2101 and LDX 2404 have been examined. 3 mm thick samples have been welded with GMAW process using three different backing gases (100% Ar, 100% N_2, 95% N_2 + 5% H_2). Results show that: for both materials, the use of nitrogen-containing backing gases produced in the root weld a slight increase in austenite content compared to the 100% argon and no-baking gas configurations, keeping a more balanced austenite/ferrite ratio. In LDX 2101, the presence of nitrogen in the baking gas showed a slight decrease in corrosion rate compared to full argon and no backing gas configuration. In LDX 2404 an increase in the corrosion rate was observed in samples welded with the three different backing gases, compared to the no backing gas sample, with a remarkable pitting corrosion observed in the base material.

INDICE

INTRODUCTION

Stainless Steels (also known as Inox steels) are defined by the European Norm EN 10088 as ferrous alloys with a minimum of 10.5% chromium content by mass.
The main property that makes this kind of materials irreplaceable is their excellent corrosion resistance in aggressive oxidizing environments, given by their high Chromium content.
This corrosion resistance is due to the formation of a thin layer of Chromium oxide (Cr_2O_3) when the material is exposed to oxygen; the phenomenon is called "passivation". This special film, which is about 1-10 nm thick, protects the material underneath from oxidation, remarkably reducing the corrosion rate. Furthermore, it can quickly regenerates when scratched.
As mentioned before, the base requirements for this behaviour are a composition with more than 10.5% of Chromium and an oxidizing environment. In any other case the passivation cannot occur.

Stainless steels are divided in four different categories depending on the microstructure:

1. Ferritic stainless steels have a stable ferritic structure at room temperature, which is a body-centred cubic (BBC) crystal structure with Chromium content between 10 - 30% and low content of C and Ni. They generally have better mechanical properties than austenitic stainless steels but worse corrosion resistance, due to the low content of Cr – Ni.
2. Austenitic stainless steels have a stable austenitic structure at room temperature, which is a face-centred cubic crystal structure. They have a minimum chromium content of 18% and Nickel of 8%, in order to keep the austenitic structure from the melting point until the cryogenic temperature. They generally present high corrosion resistance but they are expensive due to the high content of Ni.
3. Martensitic stainless steels have generally a chromium content around 12 - 15%, and high content of carbon, around 1 - 1.2%. They have the best mechanical properties like strength ant toughness, which can also be increased with heat treatments, but they have not a good corrosion resistance if compared with other stainless steels.
4. Duplex Stainless Steels have a balanced austenite-ferrite microstructure with a ratio near 50-50%. They are characterized by a Chromium content between 19 – 32% and Molybdenum up to 5%, with a relatively low content of Ni. This particular microstructure allows them to have almost twice the strength than an Austenitic stainless steel, improving simultaneously Pitting and Crevice corrosion resistance.

The purpose of the present work is to investigate the phase transformation that occurs in some of the most used Duplex stainless steels due to heat treatments and welding processes, highlighting the effects in the microstructure, corrosion resistance, and mechanical strength of the selected materials. The different subjects are developed as follows:

- Chapter 1 analyses the effect of two different heat treatments (T=800°C, T=850°C) on the microstructure and mechanical properties of SAF-2507 Super Duplex grade, focusing on the eutectic decomposition of ferrite into sigma phase and secondary austenite. A complete magnetic analysis (Stäblein-Steinitz, Eddy Current, Fischer-Ferrite), Hardness test, OM analysis are performed;
- Chapter 2 investigates the effects of Nd: YAG laser welding on the microstructure of SAF-2507 SSDS samples, putting the attention on ferrite-austenite ratio. Knowing from earlier works that previous deformation can enhance ferrite decomposition, the experiment was conducted in samples with seven different grade of deformation (i.e. ε= 0, 10, 20, 30, 40, 50, 60%). Microhardness test, Eddy current test and Corrosion test are conducted in the welded samples;
- Chapter 3 focuses on the Effects of Nitrogen-contaning backing gas on microstructure and corrosion resistance of the recently developed Lean Duplex grades LDX 2101 and LDX 2404. OM analysis, Fischer ferrite, Image analyser and Corrosion test are conducted in the root side of the welded samples.

The choice of these topics was dictated by the growing use of these Duplex steels among industries, due to their high mechanical properties and resistance to corrosive attack. These properties make them particularly suitable and competitive for applications in aggressive environments, also as structural materials. However, there are limitations to the use of duplex steels, due to microstructural transformations that may arise during the exposure of the material to high temperatures or that may occur during welding processes, compromising these attractive features.

This Master project has been carried out at the BME - Budapesti Műszaki és Gazdaságtudományi Egyetem – University of Budapest, Department of Science and Engineering Materials under the supervision of Dott. Mészáros István and PhD students Varbai Balázs and Bögre Bàlint.

CHAPTER 1

DUPLEX STAINLESS STEELS

1.1. INTRODUCTION

Dupelx Stainless steels (DSS) are a particular category of stainless steels with a biphasic microstructure (so-called Duplex) made by ferrite and austenite in almost equal volume fraction. This balanced ratio between the two phases allows reaching a very remarkable combination of mechanical and corrosion resistance properties, making these materials strongly competitive against ferritic and austenitic grades [1]–[3]. In particular, DSS have almost twice the strength compared to austenitic stainless steels and also a better pitting and stress cracking corrosion resistance. These properties are obtained with a lower alloy content than the equivalent austenitic grades, making them also cost-effective.

In order to obtain this precise microstructure, composition and solidification processes are of fundamental importance.

When a DSS solidifies from the melted state, it turns into a completely ferritic structure. As it cools down to room temperature, if the cooling rate is suitable, half of the ferritic phase transforms in austenitic phase. The result is a balanced structure with a ratio near to 50-50% (Fig. 1).

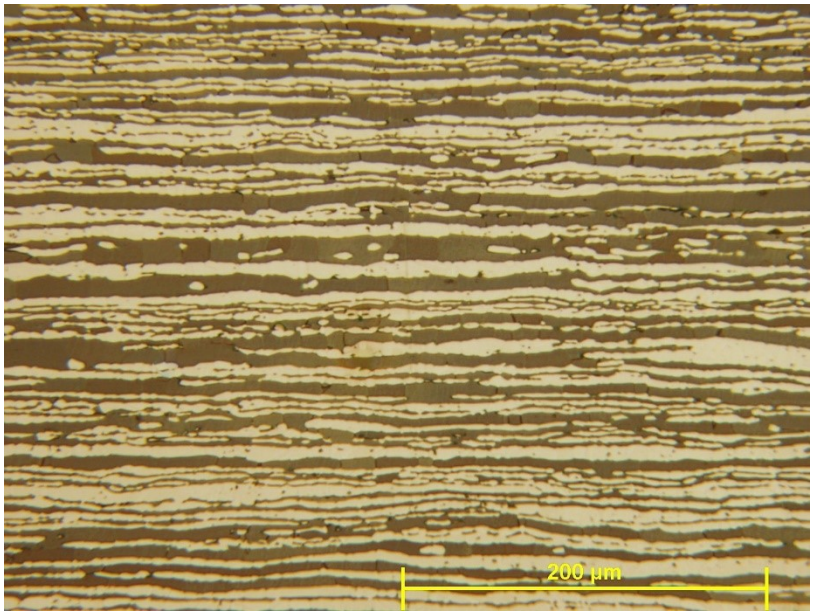

Fig. 1 Typical microstructure of a rolled UNS 32750 SDSS (clear phase: austenite; dark phase: ferrite)

DSSs are high-alloyed steels. They mainly contain chromium (18-32%), nickel (1-7%), molybdenum (5% maximum) and nitrogen (up to 0.4%), while carbon content is kept below 0.03% [1], [2], [4].
Besides the interesting properties provided by the biphasic microstructure, DSS can be efficiently employed only within a limited temperature range (-50–250°C). In fact, at lower temperatures there is a remarkable drop in toughness, whereas at higher temperatures the ferrite phase starts to be unstable, causing the precipitation of secondary phases. These precipitates hardly affect the excellent properties of the material, enhancing localized corrosion and decreasing hardness and strength [1], [2], [5], [6].

1.2. HISTORY

The growth of Duplex Stainless Steels started at the beginning of the 30's in the France and Scandinavian areas. Bain and Griffith [7], in 1927, mentioned for the first time the existence of a biphasic steel composed by austenite and ferrite, focusing on the corrosion benefits that could be obtained compared to the most common austenitic stainless steels.
Thanks to this publication, many foundries started to test duplex materials. In 1929 Avesta Steelworks produced the two first commercial grades: firstly the 453E (25% Cr, 5% Ni), used in high temperature application, e.g. for molten lead equipment and for pyrite kiln inserts. Then, the 453S, (25% Cr, 5% Ni, 1% Mo), used to make autoclaves for gunpowder production (Fig.2) and valves for sulphite pulping [7][2].

Fig. 2 Autoclave in 453S for gunpowder production [2]

In 1936, the French J. Holtzer Steelworks made a 20% Cr, 8% Ni, 2.5% Mo and 1.5% Cu grade, named Uranus 50 [8], which was found to be insensitive to intergranular corrosion in various corrosive liquid, unlike austenitic stainless steels. This corrosion resistance, combined with the higher strength compared to the austenitic grades promoted the application of DSSs, particularly for use in the pulp and paper industry. In Sweden, numerous Steelworks started to manufacture a 26% Cr, 5% Ni, 1.5% Mo grade, which was included in the Swedish standard (SIS 2324) in 1947 and later in the American standards as AISI 329.

In those years, despite these evident advantages, these innovative materials still suffered from a bad reputation regarding crack sensitivity.

For this reason, the marketing of semi-finished duplex product started only in 50's, with the introduction of Sandvik 3RE60 (18.5% Cr, 5% Ni, 2.7% Mo) and AISI 329 (25% Cr, 5% Ni, 1.5% Mo), considered as the precursors of the modern duplex stainless steels.

Development and usage of Duplex increased remarkably during the 70's thanks to two main reasons. Firstly, because of a huge shortage of Nickel that increased the austenitic stainless steels price. Secondly thanks to the introduction of new innovative techniques for the production of steel as VOD (vacuum oxygen decarburisation) and AOD (argon oxygen decarburisation). These new techniques allowed to obtain an austenite-ferrite structure perfectly balanced, with low content of residual elements (carbon, sulphur, oxygen etc.), substantially increasing the corrosion resistance and the strength of this materials.

These results, together with the introduction of continuous casting process, led to a significant saving in production costs.

Late in the 70's in Germany and Sweden was developed the well-known 2205 Grade (22% Cr, 5% Ni) that was a commercial breakthrough for DSSs. The diffusion of this steel in gas, oil and offshore industries was massive, thanks to its optimal mechanical properties, corrosion resistance and weldability.

During the 80's the need of new materials to withstand extremely aggressive environments led to the development of more highly alloyed duplex, the so-called Super Duplex stainless steel (SDSS), with a basic composition around 25% Cr, 7% Ni, 3% Mo.

In recent years, a new class of low-alloyed duplex, called Lean Duplex, has been developed in order to replace the traditional austenite grade AISI 304 – AISI 316 for applications where high resistance to stress corrosion cracking and good mechanical properties are required. The most famous grade is the SANDVIK 2304 [9] [10] [5].

1.3. CLASSIFICATION

As austenitic and ferritic stainless steels, DDSs can be classified according to their resistance to localized corrosion, which can be estimated using PREN index (Pitting Resistance Equivalent Number). PREN is a parameter that depends only on the composition of the steel, and it is commonly used to compare different grades. The expression of PREN is defined as follows:

$$PREN = \%Cr + 3.3 \cdot \%Mo + k \cdot \%N \qquad (1.1)$$

the constant *k* can assume a value between 10 and 30, but the most widely used for duplex is 16 [1], [2], [4].
For DSSs that contain also tungsten, in order to take into account the increasing of corrosion resistance given by this alloy, the relation (1.1) changes [11] as follows:

$$PREW = \%Cr + 3.3 \cdot \%Mo + 1.65 \cdot \%W + k \cdot \%N \qquad (1.2)$$

The use of PREN (or PREW) is qualitative, because it considers only the nominal composition of the steel without taking into account the different elements partitioning between austenitic and ferritic phase.

Table 1 Chemical composition and PREN index of most common DSSs

Standard	Company	Trade name	C	Cr	Ni	Mo	N	Cu	W	Remarks	PREW
UNS S32304	Sandvik[2]	SAF 2304	0.03	23	4	0.2	0.1	0.2	-		25
"	Cr. Loire	UR 35N									
UNS S31803	Sandvik	SAF 2205	0.03	22	5.2	3.1	0.18	-	-	N:0.08-0.20	35
	Avesta-Sheffield	2205									
	Cr. Loire	UR 45N	0.03	22	5.5	3	0.15	-	-		34
	Cr. Loire	UR 45N+	0.03	22.8	6	3.3	0.18	-	-		36
	Krupp Stahl	FALC 223	0.03	22	5.3	3	0.17	-	-		35
	DMV	AF22	0.03	22	5.3	3	0.17	-	-		35
UNS S32205	Sandvik	SAF 2205	0.03	22	5.2	3.1	0.18			N:0.14-0.20	35
	Avesta-Sheffield	2205									
UNS S31500	Sandvik	3RE60	0.03	18.5	5	2.7	0.1	-	-	1.5 Si	29
	VEW										
UNS S32900	Sandvik	5RD58	0.08	25	4.5	1.5	-	-	-		30
UNS S32950	Carpenter	Carp 7Mo+	0.03	27	4.8	1.8	0.25	-	-		35
UNS S32550	Langley	Ferralium 255	0.05	25	6	3	0.18	1.8	-		38
UNS S31250	Sumitomo	DP3	0.03	25	6.5	3.0	0.16	0.5	0.3		38
	VEW	A905	0.03	26	3.7	2.3	0.34	-	-	Mn 5.8	39
	Cr. Loire	UR 47N	0.03	25	6.5	3	0.17	0.2	-		38
	Cr. Loire	UR 52N	0.03	25	6.5	3	0.17	1.5	-		38
	DMV	VS 25	0.03	25	6.5	3	0.18	-	-		38
UNS S32750	Sandvik[2]	SAF 2507	0.03	25	7	4	0.27	-	-		42
	Cr. Loire	UR 47N+									
UNS S32760	Weir	Zeron 100	0.03	25	7	3.2	0.25	0.7	0.7		41
	Cr. Loire	UR 52N+	0.03	25	6	3.3	0.24	1.5	-		40
UNS S32740	Sumitomo	DP3W	0.03	25	6.7	3.1	0.26	-	2.0		43

Furthermore, PREN number does not consider the influence of nickel content, which is known to play a role in the corrosion-resistance properties of the stainless steels [2], [4], [11].
Nevertheless, PREN (or PREW) is commonly used to classify DSS in four main categories:

1. Lean DSSs (such as LDX 2101 and LDX 2404), have a PREN value around 25. They are characterized by really low content of Ni and Mo, which are balanced by higher content of Mn and N;
2. Standard DSSs (most common the SAF 2205), have PREN around 35;
3. Super DSS (such as SAF 2507 and Zeron 100) have a PREN value that is between 40 and 42. They are high-alloyed and they offer a corrosion resistance equivalent to that of super austenitic grades.
4. Hyper DSSs (like SAF 2707) have PREN around 45, they are extremely alloyed and expensive, but irreplaceable by other stainless steels.

1.4. INFLUENCE OF ALLOYING ELEMENTS

As mentioned before, the continuing development of duplex stainless steels has resulted in complex steel compositions (see Table 1) containing significant amounts of several alloying elements. These elements are introduced in the steel in order to obtain better mechanical properties and/or higher corrosion resistance, always keeping a balanced duplex microstructure. Each alloying element have a specific effect on the properties of the steel. Therefore, is useful to present a brief overview of these elements.

Chromium (Cr)

Chromium is the main alloying element in stainless steels. It is a strong ferrite stabilizer: it promotes ferritic α-phase. A minimum of 10.5% of Cr is required to confer to the steel the passivation property that makes it “stainless”. The localised corrosion resistance (pitting, crevice) increases with increasing chromium content. Nevertheless, there is a limit to the level of chromium that can be added to the steel, as the beneficial effect of higher levels is cancelled by the increasing of precipitation of intermetallic phases (σ phase, χ phase, chromium nitride, etc.) [1], [4], [5].

Nickel (Ni)

Nickel is a strong austenite stabilizer. It is added in order to maintain a balanced austenite-ferrite microstructure. For this reason, the level of nickel content in a duplex alloy will depend mostly on the chromium content (ferrite stabilizer). It also generally increases ductility and toughness. However, excessive Ni contents can promote ferrite transformation to intermetallic phases if the alloy is exposed to

temperatures in the range 650 to 950°C. Ni does not show a direct effect on corrosion properties, and its main role is to control phase balance and element partitioning [1], [4], [5].

Molybdenum (Mo)

The main effect of adding molybdenum in the steel's composition is the increasing of pitting and crevice corrosion resistance. This is obtained thanks to the tendency of Mo to repress active sites with the formation of an oxy-hydroxide or molybdate ion. As seen before in relationships 1.1 and 1.2, Molybdenum is included in PREN/PREW index with a coefficient 3.3 higher than chromium. Furthermore, molybdenum enlarges the passive potential range and reduces the corrosion current density in the active range. An addition of at least 3% Mo is required in high temperature seawater to prevent crevice corrosion, while an upper limit of about 4% Mo is recommended to restrict σ phase precipitation in hot working temperature above 1000°C [1], [4], [5].

Nitrogen (N)

Nitrogen is one of the strongest austenite stabilizer elements. As Mo, it has an important role in increasing pitting resistance and extending the passive potential range. The coefficient of nitrogen in the PREN/PREW relationship (1.1, 1.2) varies between 13 and 30, but the most widely used value for duplex alloys is 16. It has been found that Mo and N have a synergistic influence on pitting characteristics and also increases the crevice corrosion resistance by altering the crevice solution chemistry or by segregating to the surface. Nitrogen mainly dissolves into austenite phase because of the increased solubility in that phase and concentrates at the metal-passive film interface.

Another fundamental effect of N is to stabilise duplex alloys against the precipitation of intermetallic phases (σ phase, χ phase, chromium nitride, etc.) by reducing chromium partitioning. Moreover, increasing the nitrogen level actually reduces the risk of nitride formation. This is due to an increase in austenite content and so a reduction in the distance between austenite islands. The addition of N is also suggested to strengthen both ferrite and austenite by interstitial solid solution. Finally, as nitrogen is a strong austenite stabiliser, its addition in shielding/backing gases during welding processes is recommended in order to keep the balanced austenite/ferrite ratio in the WZ and HAZ [1], [4], [5].

Manganese (Mn)

Manganese has an effect on the ferrite/austenite balance that varies with temperature: at low temperature, it is an austenite stabilizer, while at high temperatures it stabilises the ferritic phase. However, no significant effect has been observed with the normally used quantity. If Manganese increases the solubility of nitrogen, on the other hand it also extends the temperature range and formation rate of detrimental σ phase. Mn addition to stainless steel increases abrasion and wear

resistance and tensile properties without loss of ductility. Further, the combined addition of Mn and N enhances the pitting resistance [1], [4], [5].

Copper (Cu)

Copper is used in high-alloyed austenitic stainless steel to reduce the corrosion rate in non-oxidising environments, such as sulphuric acid. In DSSs, the addition of Cu is limited to about 2%, because higher levels decrease hot ductility and can lead to precipitation hardening. Cu is suggested to enhance machinability in low oxygen and sulphur materials and can lead to hardening after exposure to the 300–600°C temperature range [1], [4], [5].

Tungsten (W)

As pointed out in relation 1.2, tungsten addition is seen to improve pitting resistance, by extending the passive potential range and reducing the passivation current. Moreover, W has been noted to increase crevice corrosion resistance in heated chloride solutions, because of its adsorption in the passive layer. The addition of tungsten is limited around 2%, in order to restrict the intermetallic formations that happen between 600 and 1000°C [1], [4], [5].

Carbon (C)

Carbon is a strong austenite stabilizer generally used to balance the microstructure and increase the mechanical strength. Carbon content in DSSs is limited to 0.02-0.03% in order to restrict chromium carbides' precipitation, which can remarkably compromise the resistance to intergranular corrosion [1], [4], [5].

All the effects of alloying elements on the final microstructure of stainless steels are summarized in Schaeffler diagram (Fig.3). This empirical diagram was originally developed to predict the microstructure of welded materials knowing its chemical composition. Schaeffler divided the alloying elements in two categories, according to their tendency to promote austenitic or ferritic phase. Then he defined two parameters, Chromium equivalent (C_{eq}) and Nickel equivalent (N_{eq}), in order to evaluate the contribution of each element. C_{eq} and N_{eq} are calculated as follows [12]:

$$Cr_{eq} = \%Cr + \%Mo + 1.5 \cdot \%Si + 0.5 \cdot \%Nb + 2 \cdot \%Ti \qquad (1.3)$$

$$Ni_{eq} = \%Ni + 30 \cdot (\%C + \%N) + 0.5 \cdot \%Mn \qquad (1.4)$$

The Schaeffler diagram is an important and easy tool that allows a rough evaluation of the microstructure as a function of the steel composition; nevertheless, it does not consider the influence of the cooling rate and aging heat treatments.

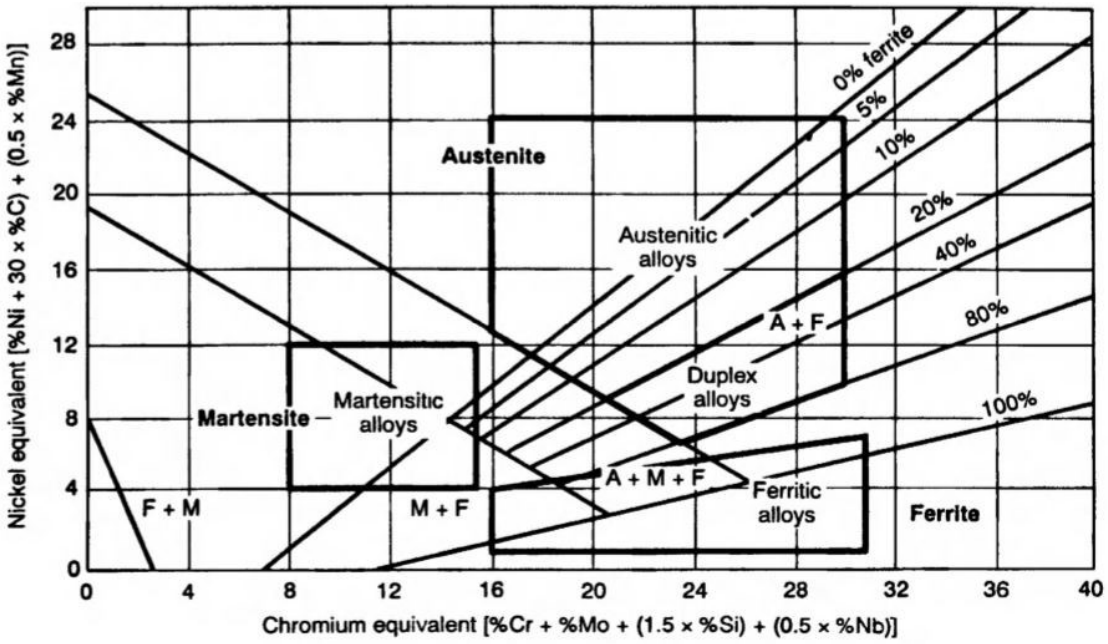

Fig. 3 Schaeffler diagram for stainless steels [2]

1.5. PHISICAL METALLURGY

Duplex stainless steels have a biphasic microstructure (Fig, 1), made of ferrite (α phase) and austenite (γ phase) in almost the same volume fraction. This particular microstructure is the key of this category of stainless steels, conferring them a remarkable combination of corrosion resistance and mechanical properties. Each phase lends a specific task: α-phase provides the mechanical strength and the resistance to stress corrosion cracking, while γ-phase guarantees a certain ductility. The result is a material with high mechanical properties and better corrosion resistance than the other stainless steels. If the biphasic microstructure on one hand allows obtaining these notable features, on the other hand brings certain intrinsic hazardous characteristics. DSSs are subjected to significant microstructural modifications because of either high temperature heat treatments or high cooling rate. The instability of the ferrite phase at high temperature may bring to the precipitation of harmful secondary phases (σ phase, χ phase, chromium nitride, etc.), while a fast cooling rate for liquid state can bring to an unbalance microstructure. These changes lead to a drastic reduction in their exceptional properties [1]–[4], [13]. In order to avoid that, it is of fundamental importance knowing the physical metallurgy, the kinetics of precipitation (of secondary phases) and the parameters that affect

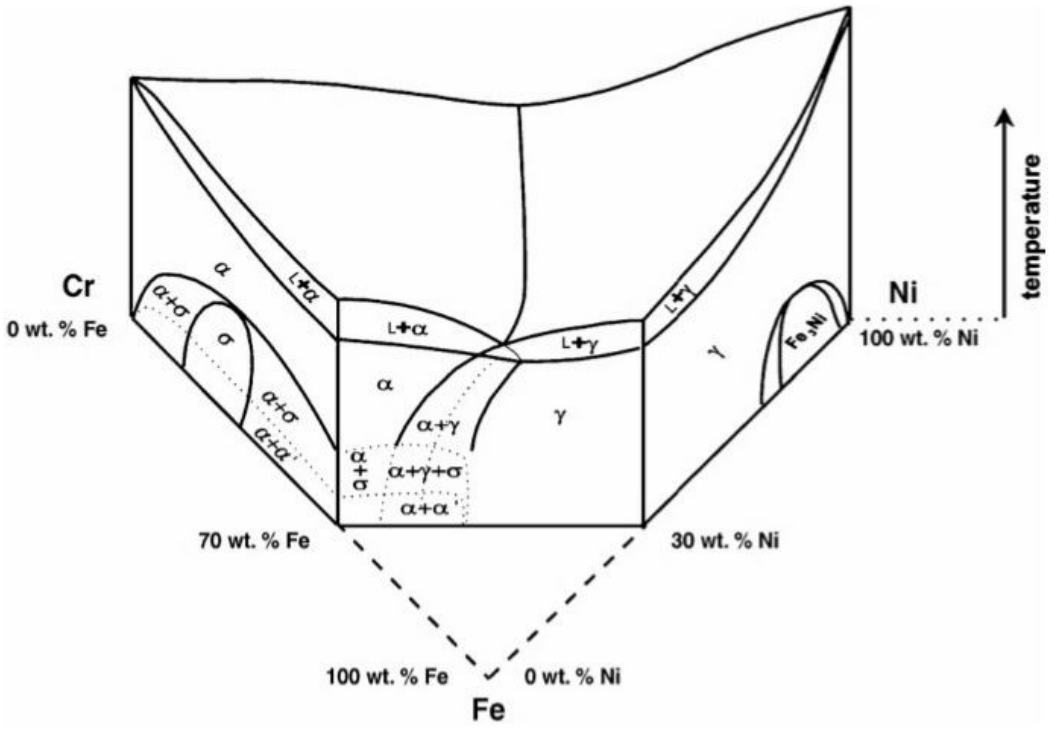

Fig. 4 3D view of the Fe-Cr-Ni equilibrium diagram [2]

the microstructure of DSSs. Since DSSs are high-alloyed steels with 6-7 main alloying elements, their behaviour related to the variation of temperature cannot be described with the ordinary state diagrams. Therefore, simplified diagrams as the pseudo-binary diagrams or sections of the ternary Fe-Cr-Ni diagram (Fig.4) can be used for studying their physical metallurgy.

Nevertheless, these representations are really onerous and give just a qualitative information, since they do not take into account all the alloying elements [14].

In last years, thanks to the improvement in computational systems and material science, various software have been developed in order to easily obtain the phase diagram for a selected system.

One of the most used is the Thermo-Calc software, developed by Sundman et all [15]. It is based on the minimization of the Gibbs free energy for the most stable phases, using thermodynamic functions interpolated by experimental data. The software allows predicting the type and the amount of phases in the DSS equilibrium microstructure. An example of a phase diagram obtained with the Thermo-Calc software is showed in Fig. 5 [6], [14]. It has been developed for a Duplex steel with a fixed composition of 7%Ni, 4%Mo and 0.3%N, with different chromium content. The dotted line inside the diagram refers to the SAF 2507 composition. As already mentioned, it is possible to see from the diagram that DSS solidifies from a liquid state in a full ferritic structure (δ) and then it turns into a duplex stable (δ + γ) microstructure between 1350 and 950°C.

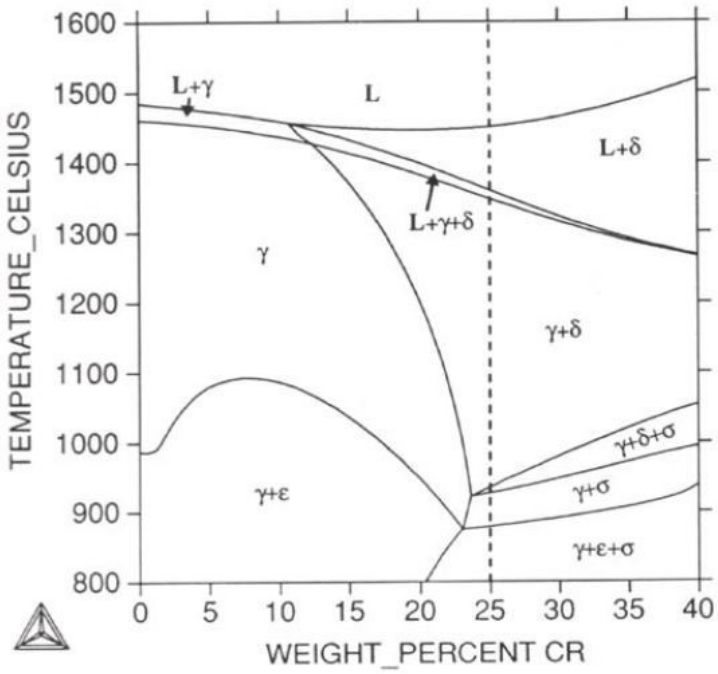

Fig. 5 State diagram for temperature above 800°C developed with Thermo-Calc software. Dotted line refers to the composition of Super Duplex SAF 2507.

1.6. SECONDARY PHASES PRECIPITATION

Due to the biphasic microstructure of DSSs, several secondary phases may precipitate in a temperature range between 300 and 1000°C. These microstructural changes can occur as a result of inappropriate heat treatments or unsuitable cooling rates, and are a direct consequence of ferrite instability at high temperatures (T<950°C, as shown in Fig.5). The intermetallic phases start forming at austenite-ferrite boundaries, which are nucleation sites characterized by lowest interface energy, and then grow inside ferrite grains, in which diffusion processes are 100 times faster than in austenite. As these compounds are rich of chromium and molybdenum, surrounding areas result depleted of these elements, remarkably decreasing localized corrosion resistance. Furthermore, they have a detrimental effect also on ductility and toughness of duplex steels.
It is well known that also the chemical composition have a fundamental role on the precipitation kinetics. Alloying elements as Cr, Mo, Cu and W promote the precipitation and enlarge the stability range of intermetallic compounds. Fig.6 shows the TTT diagram for a generic Duplex. Two main temperature ranges can be recognized as highly dangerous for secondary phases precipitation:

1. The low-temperature range, between 300 and 600°C, which is known as “475°C embrittlement”. This range is mainly characterized by the spinoidal decomposition of ferrite in domains respectively rich and poor of Cr, with

slight different lattice parameters. Another important transformation in this range concerns G-phase precipitation, an intermetallic compound full of Ni, Mo and Si. The final results is a remarkable embrittlement of the material, which is the reason why DSS applications are restricted to temperatures lower than 280°C;

2. The high-temperature range, between 650 and 1000°C, during which occur the eutectic decomposition of ferrite into σ phase and secondary austenite. Besides these two, many other secondary phases may precipitate in this range: intermetallic compounds, carbides, nitrides. The precipitation kinetics and the incubation time are highly affected by the chemical composition of the steel. For this reason, high-alloyed steels like Super/Hyper Duplex are extremely sensitive to these precipitations. The result is a remarkable decreasing in both mechanical and corrosion resistance properties.

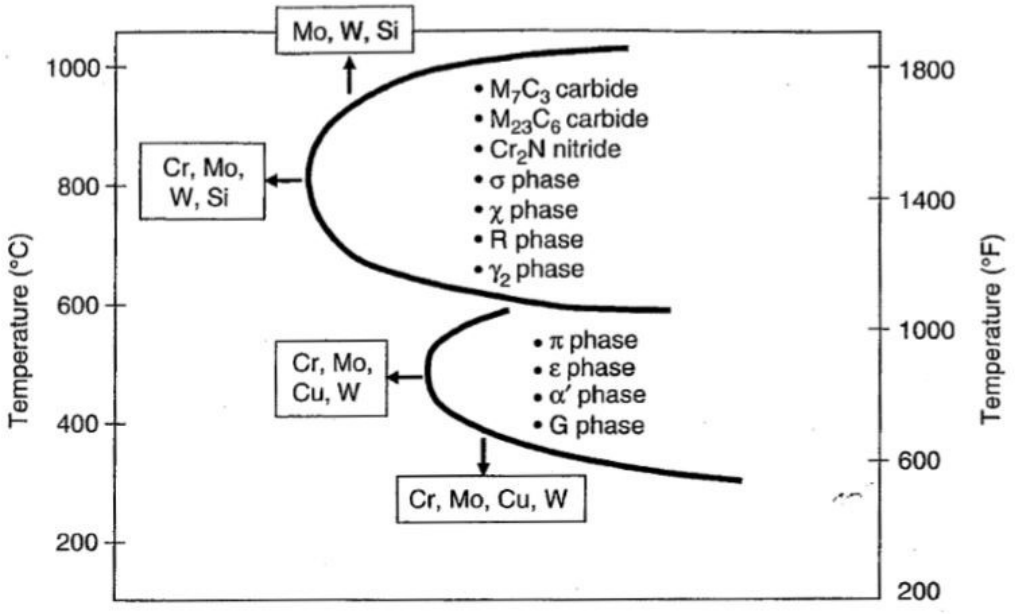

Fig. 6 Secondary phases range in DSS and influence of alloying elements on precipitation kinetics [16]

Sigma phase (σ)

Sigma phase is the most important precipitate that grows in the 650-1000°C range. It originates from the eutectic decomposition of ferrite, that being metastable in this range, turns into a more stable mixture of sigma phase and secondary austenite ($\alpha \rightarrow \sigma + \gamma_2$). It precipitates preferentially at austenite/ferrite grain boundaries, and grows toward ferritic grains. The formation of σ is mainly favoured by Cr and Mo (Fig 6), which enlarge its stability field and enhance both the precipitation rate and its volume fraction. At the peak temperature of 850°C, the incubation time for DSSs is estimated in just few minutes. It may precipitate in every duplex grades, and it has

deleterious effects on corrosion resistance and impact toughness, even if present in very small amounts.

The σ-phase is a hard and brittle phase; its unit cell does not possess easy-slip planes, therefore it causes remarkable embrittling effects. Because of its composition (Tab.2), its formation causes a depletion in chromium of the surrounding area, whose composition drops below the passivation upper limit, facilitating the localized corrosion mechanisms in the area adjacent to the precipitated particles. [8]–[12], [22], [23]

.

Table 2 Chemical composition of sigma phase (σ) [4]

Cr	Ni	Mo	W
29-34	3-5	3-9	0-7

1.7. APPLICATION

DSSs are used in all that kind of applications where both high strength and excellent corrosion resistance are required. One of the most important employment of these materials is the oil and gas industry. The offshore extraction in seawater and the transportation of natural resources, containing high content of CO_2 and H_2S, requires corrosion-proof flowlines. Nowadays, more than 1000 km of welded duplex flowlines are installed globally, most of which are made in 2205, with some application of Super Duplex grades.

Another important field of application regards pulp and paper industry. In this area, DSSs are commonly used for pulp digester, in which the hot alkaline environment increases risk of stress crack corrosion. They are applied also in the construction of hydrogen peroxide reactor (Fig 7) for bleaching process, where duplex steels are

Fig. 7 Hydrogen peroxide reactor made in LDX 2101 (2006) [2]

the perfect material to handle high temperature and pressure together with the high alkaline environment. In this particular application, the usage of the rather newly developed lean duplex grade LDX 2101 is increasing.
DDSs are widely used in the construction of mobile and storage tanks (Fig 8) [18]. In this field they are preferred to austenitic grades because, having higher strength, they allow saving a large amount of weight (which is estimated to be around 25-30%). The choice of the duplex grades is made depending on the aggressiveness of the storage liquid, but Lean duplex grades are frequently used for these applications.

Fig. 8 Duplex storage tanks in LDX 2101 for liquids hazardous to water [18]

In recent years, the interest in DSS is considerably growing also among construction companies. These materials can guarantee low maintenance and the low life-cycle cost (LCC), allowing to increase lifetime and limit the repairs costs.
Nevertheless, also if they have already been used in the construction of large welded bridges (Fig 9), their application is limited. This is due to lack of experimental data on DSS fatigue resistance, when compared to the well-established theory for carbon steels [1],[2],[4],[5],[13].

Fig. 9 Apatè bridge in Stockholm made of duplex 2205 [4]

CHAPTER 2

DECOMPOSITION KINETICS OF FERRITE IN ISOTHERMALLY AGED 2507 SDSS

2.1 INTRODUCTION

As mentioned in the previous chapter, due to biphasic microstructure and the high amount of alloying elements, SDSSs are strongly affected by precipitation of harmful secondary phases (σ phase, χ phase, chromium nitride, etc.) if they undergo inappropriate aging treatments [19]–[24].
These phase transformations mostly regard the ferritic phase, because the diffusion rate of ferrite's elements is 100 faster than austenite one. For this reason, the precipitates are mainly composed by Cr and Mo and their growth results in a depletion of these elements in the ferritic matrix, compromising the local corrosion resistance and the mechanical properties of these materials [19], [24].
The most important precipitate is the σ phase because of its drastic impact on ductility and toughness of DSS. It is generated between 650 and 1000°C by the eutectic decomposition of ferrite, where the metastable ferritic α-phase turns into a more stable mixture of sigma phase and secondary austenite according to the following equation: $\alpha \rightarrow \sigma + \gamma_2$.
Even though many authors have studied the decomposition of ferrite in duplex stainless steels due to aging treatments, further information is still needed to provide a complete understanding of this complex metallurgical process.
In the present chapter, the decomposition kinetics of ferritic phase (α) in isothermally aged UNS S32750 (2507) SDSS is studied in the range of 800-850°C.
This range, in according with the time-temperature-transformation (TTT) diagram, is the most critical for the formation of σ phase [19].

2.2 MATERIAL AND EXPERIMENTAL PROCEDURE

2.2.1 MATERIAL AND SAMPLE PREPARATION

The investigated material is the UNS S32750 (SAF2507) SDSS. It was supplied by ARCELORMITTAL. Its chemical composition can be found in Table 3.

Table 3 Chemical composition of SDSS 2507

Element	C	Mn	P	S	Si	Cu	Ni	Cr	Mo	N
%	0.021	0.822	0.0231	0.0004	0.313	0.178	6.592	24.792	3.705	0.2644

The as-received material was a sheet of 13mm thickness, previously solution annealed at 1100°C and water quenched. From this sheet material, 20x20 mm samples were cut for the heat treatments.
The samples were isothermally heat treated at 800 and 850°C in a pre-heated electric furnace. The times of treatment are reported in Table 4. The heating time needed by the samples to reach the aging temperature has been neglected. Thus, the ones reported correspond to the actual time that the samples stayed inside the furnace. After that, all the specimens were placed on a ceramic block and left cooling down at T=20°C.

Table 4 Aging time for the two temperatures of treatment

Heat treatment temperature (°C)	Time of treatment (min)									
800	0	5	10	15	30	42	58	73		
850	0	5	10	15	20	25	30	35	40	45

In order to allow a correct investigation of the cross surface, all the samples were grounded with SiC abrasive papers with decreasing grit size (P80, 120, 320, 600, 1200, 2400) and then polished with clothes (3μ and 1μ) using polycrystalline diamond suspension.

2.2.2 OM ANALYSIS

The optical microscope technique is usually the first investigation made in the micrographic examination of a metallic material. It is widely used because it allows to recognize very easily the phases present in the material structure, the proportion between them and their size and distribution. It is also very useful for discovering the precipitate that may develop in the microstructure, and at the same time to find the presence of material defects as porosity, cracks and any kind of non-metallic inclusion. It does not give any information about the chemical composition of the discovered phase. Therefore, the microstructure of the material must be known beforehand to correctly analyse the results. The OM technique is characterized by a low resolving power, less than 0.2 μm. For this reason, only large precipitates like σ phase can be observed, while smaller one like chromium nitride are undetectable. After the polishing process, a chemical attack of the samples' surface is required in order to analyse the microstructure. This process is necessary because, due to the polishing, the surface results to be completely specular and does not allow any metallographic analysis. Therefore, the chemical attack, called etching, must be done to highlight the different phases. It is of fundamental importance to select the appropriate chemical reagent for the etching to obtain the best results [22].

For our samples we decided to use the Beraha reagent which gives an optimal contrast between the phases, making the ferrite dark and the austenite clear. Chemical composition and etching conditions are given in Table 5.

Table 5 Composition and etching conditions used for the OM analysis

Chemical reagent	Chemical composition	Etching contitions
Beraha	- 85ml H_2O - 15ml HCl - 1g $K_2S_2O_5$	- Time of etching: 30s - Temperature: 20°C

After the etching process, the analysis was executed with the OLYMPUS PMG 3 microscope in five different magnification (25x – 100x – 200x – 500x – 1000x). Pictures were taken for every samples.

2.2.3 VICKERS HARDNESS TEST

The Hardness is considered as the resistance that a material shows to plastic deformation caused by indentation. Hardness test is the most valuable and most used mechanical test for characterizing mechanical properties of metals or alloys. This test is preferred because it is simple, and relatively non-destructive, and because it gives an immediate evaluation of the mechanical properties of the studied material. At first, the sample's surface is indented with a diamond indenter in the form of a square-based pyramid with an angle of 136 degrees between opposite faces (fig. 10).

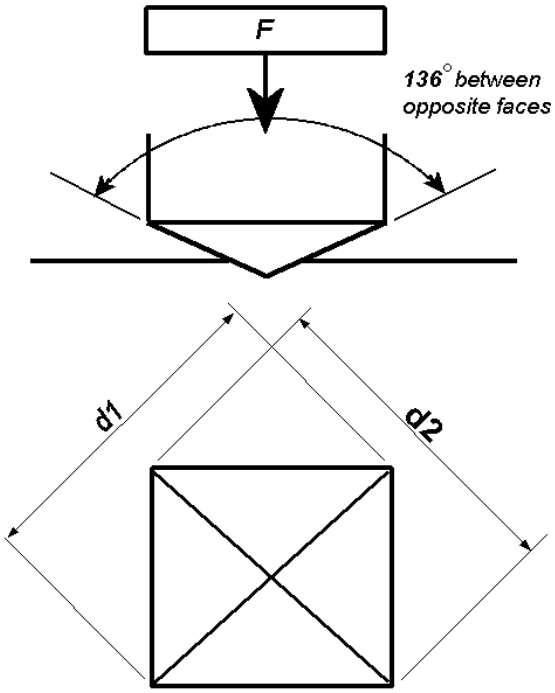

Fig. 10 Indentation geometry and shape [25]

Through the indenter, the material is subjected to a load (F) between 1 and 100 kgf with an application time that usually goes from 10 to 15 seconds. After that, the two diagonals of the indentation left in the surface (Fig. 10) of the material are measured using a microscope; then their averaged value (d) is calculated. The Vickers (HV) number is then determined by the following equation:

$$HV = 1.854\frac{F}{d^2}\left[\frac{Kgf}{mm^2}\right]$$

When F is in N, the constant change to 0.1891.
The hardness test was done in according with the ISO 6507-1:2005 standard using a KB-Prüftechnik 250 BVRZ with a load of 10 kg and an application's time of 12s. For each sample, 5 hardness measurements were carried out on the polished surfaces, from which average and standard deviation were calculated.

2.2.4 MAGNETIC TESTS

Magnetic tests are a powerful instrument for studying duplex stainless steels, since they are highly sensitive to the amount and the structure of ferromagnetic ferrite phase. Therefore, they are suitable for studying the eutectic decomposition that occurs during the aging treatments.
Previous studies confirmed that magnetic saturation (B_s) is proportional to ferrite content [19], [22] and that coercive force (H_c) increases with the amount of precipitations, like the σ-phase [19], [25].
In this work, three different magnetic tests have been adopted, namely: Stäblein-Steinitz, Fischer Ferrite and Eddy current test.

2.2.4.1 Stäblein-Steinitz test

Stäblein-Steinitz tester is a DC close magnetic circuit built to reach high magnetization field. It is used for studying the Hysteresis loops of samples with small ratio of length to transverse dimensions.
As shown in Fig.11, the tester is composed by two symmetrical U-shaped Iron yokes (10x10 cm) placed opposite to each other, with an air gap between them that varies from 0 to 50 mm. In both yokes a magnetizing coil is placed at the end of each arm. The coil is supplied with sinusoidal (10 Hz) exciting current produced by a function generator and a driving amplifier. The set-up contains a so-called bridge-branch in the middle of the arms, which is flux less because of the symmetry of the circuit. Upsetting the symmetry by placing a specimen in the air gaps between the faces of the yokes, produces a flux in the bridge-branch's air gap. For measuring it, two magnetic hall sensors are placed inside the circuit, one in the air gap situated in the bridge-branch, another under the sample (Fig. 11).The flux of the bridge-branch can be calculated by a simple concentrated parameter model of the magnetic circuit. After the proper simplifications, it results:

$$\mu_0 M_{sample} = B_{Bridge} \frac{C_1 \left(1 + \frac{C_2}{l}\right)}{A}$$

Where L and A are respectively the length and the cross section of the sample, while C1 and C2 are constant determined during the calibration of the tester. This demonstrates that the magnetic polarization of the measured sample is linearly proportional with the magnetic induction detected within the bridge-branch [26].

The first step of our test was the *calibration* of the double yoke magnetometer. This step is of fundamental importance in order to obtain useful results. A correct calibration of the tester is reached when the system produces, without samples, a horizontal line.
Once the calibration was achieved, before every measurement a *demagnetization process* was done in the samples (Fig.12).

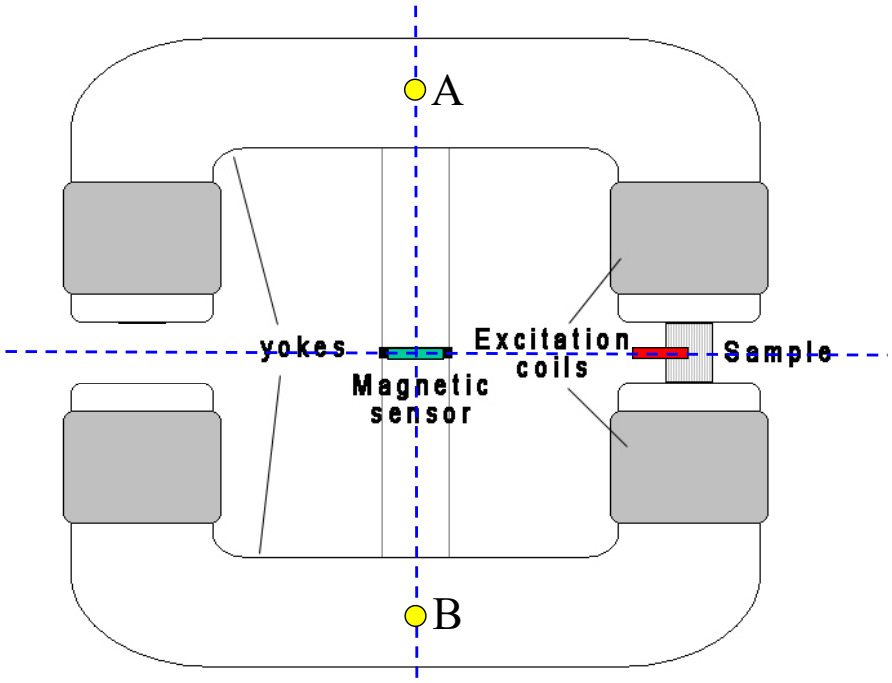

Fig. 11 Stäblein-Steinitz set up

To measure correctly the hysteresis loop, we must start with a demagnetized sample in which H and B are simultaneously equal to zero. Demagnetization is accomplished by subjecting the sample to a series of alternating fields of slowly decreasing amplitude. In this way, the induction is forced to traverse smaller and smaller loops until it finally arrives at the origin [27].

At the end we measured the hysteresis loop (Fig. 13) for every sample, from which we derived the values of magnetic saturation (B_s) and Coercivity (H_c).

The magnetometer works under full control of a personal computer; the measurement are accomplished by an input-output data acquisition card (DAQ). The data acquisition, processing and the control of the set-up were done by using "LabView VI".

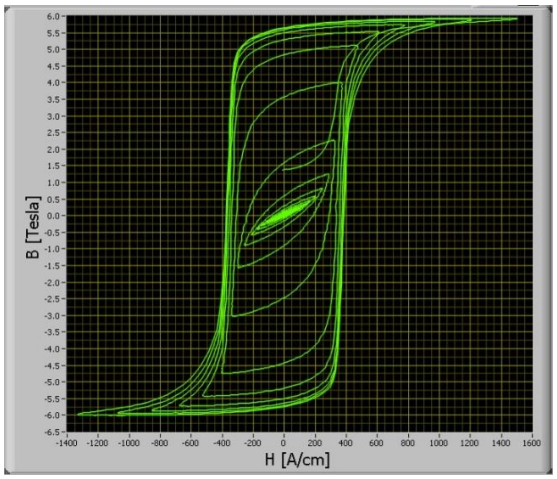

Fig. 12 Demagnetization process

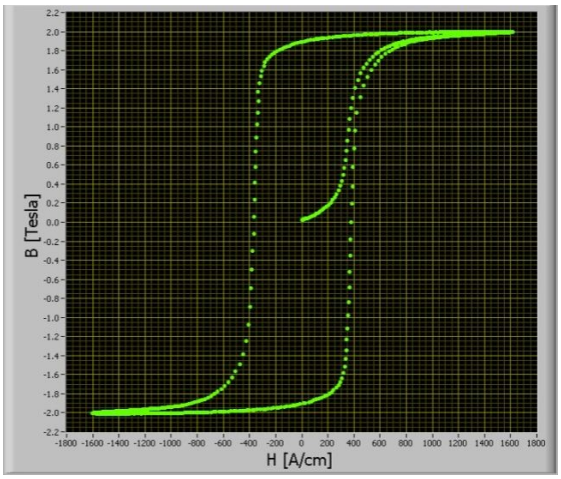

Fig. 13 Hysteresis loop

2.2.4.2 Fischer Ferrite test

Fischer Ferrite test is one of the most widely used magnetic test for the measurement of ferrite content in duplex stainless steel. Its success is due to ease of use and directness in providing results. In fact, the measurement only consists in placing the instrument's probe above the surface of the sample. Then, the Ferrite content is instantaneously shown in the display of the device as ferrite content (%) or ferrite number (FN).
For our measurements, we used the FERITSCOPE FMP30 produced by Fischer, which measures according to the magnetic induction method. A magnetic field, generated by a coil, begins to interact with the magnetic portions of the specimen. The change in magnetic field induces a voltage proportional to the ferrite content in a second coil, as visible in Fig. 14. This voltage is evaluated by the instrument and translated in ferrite content.
Being a portable instrument powered by 4 AAA 1.5V batteries, the Feritscope cannot produce a magnetic field strong enough to saturate the ferromagnetic ferritic phase. Therefore, the measurement of the ferrite content is obtained through the measurement of the initial permeability (μ_i) of a minor hysteresis loop. Nevertheless, the results of this test are highly used by scientific community and by industries.
For our test, three measures were taken in each surface of the samples (four sides, two faces).

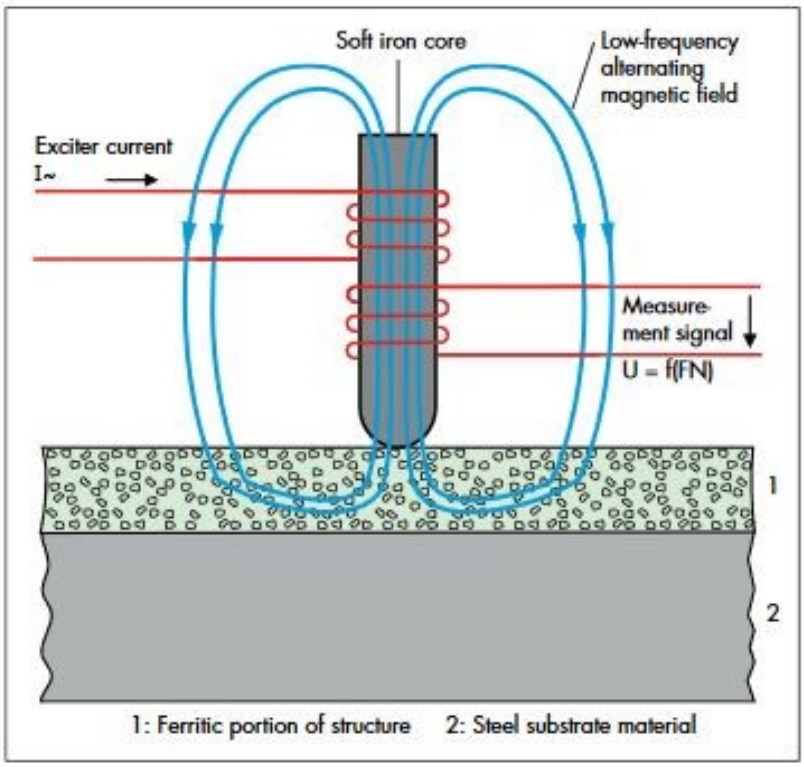

Fig. 14 Operating principle of the magnetic induction measurement method [13]

2.3 RESULTS

2.3.1. OM ANALYSIS

With the optical microscope analysis we could clearly observe the eutectic decomposition of the ferrite phase (dark) in secondary austenite and σ-phase (white) for both the aging treatments (T=800°C, T=850°C).

The microstructures of the samples aged at T=800°C for 0, 30, 42 and 72 minutes is shown in Fig. 15. Before the heat treatments the microstructure contained only ferritic and austenitic phase grains, in approximately equal fraction (Fig 15.a). σ-phase started to precipitate after 30 min of treatments, exclusively on the boundaries of α/γ grains (Fig 15.b). As the aging time increased, the precipitates started to penetrate into the ferrite grains (Fig 15.c). After 72 min of treatment (Fig. 15.d) ferrite phase is almost completely disappeared, and the microstructure contains only austenite (primary and secondary) and σ-phase.

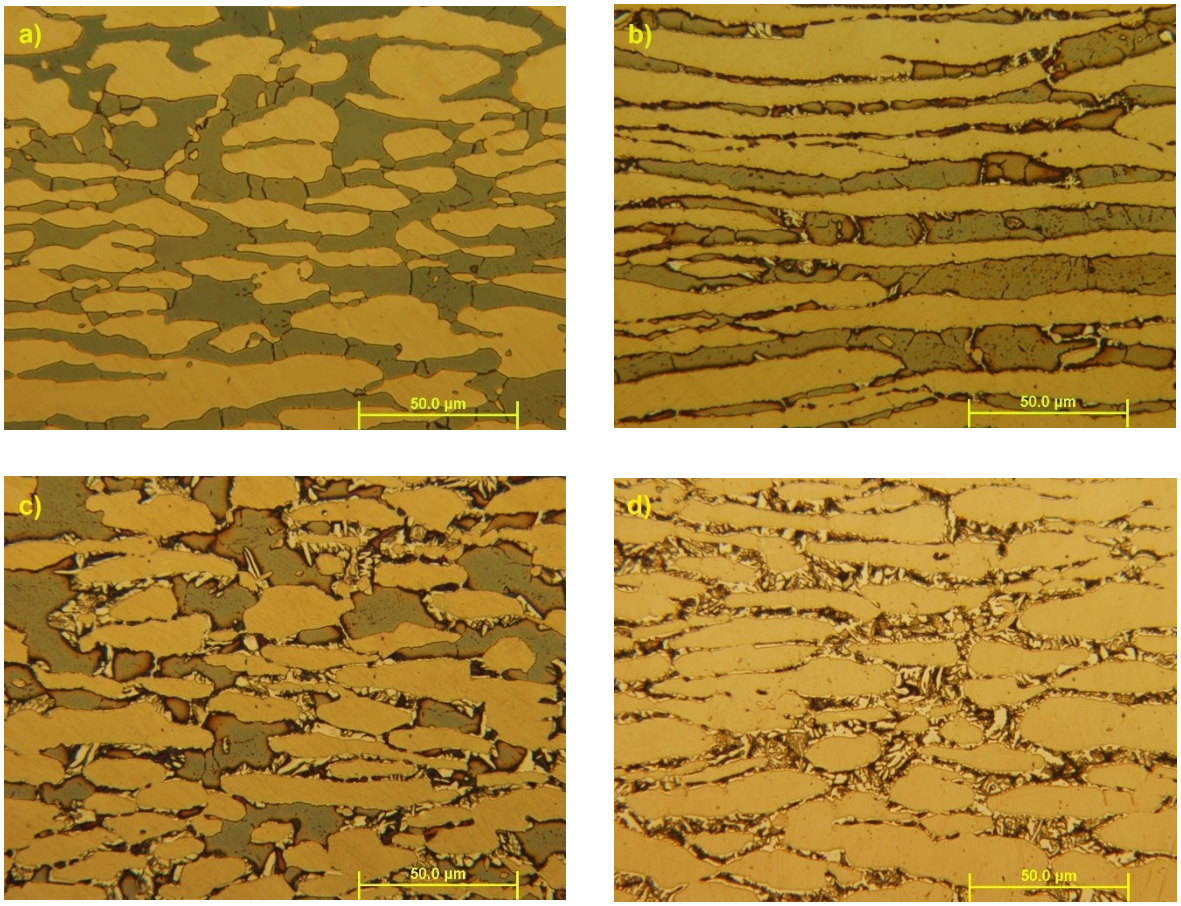

Fig. 15 Microstructure evolution of the samples isothermally aged at T=800°C for different time: a) no heat treated; b) t=30 min; c) t=42 min; d) t=72 min.

The microstructure transformation for the samples isothermally aged at T=850°C followed the same evolution seen for the treatments at 800°C, but with a precipitation time significantly shorter.
As can be seen in Fig. 16, σ-phase started to grow on the ferrite/austenite junction already after 5 minutes (Fig. 16.a). Increasing the aging time, the amount of σ increased at the expenses of the ferritic phase (Fig. 16.b, 16.c). Some precipitates can be seen also inside the austenitic grains. After an aging time of 35 minutes (Fig. 16.d), almost all the ferrite phase has decomposed.

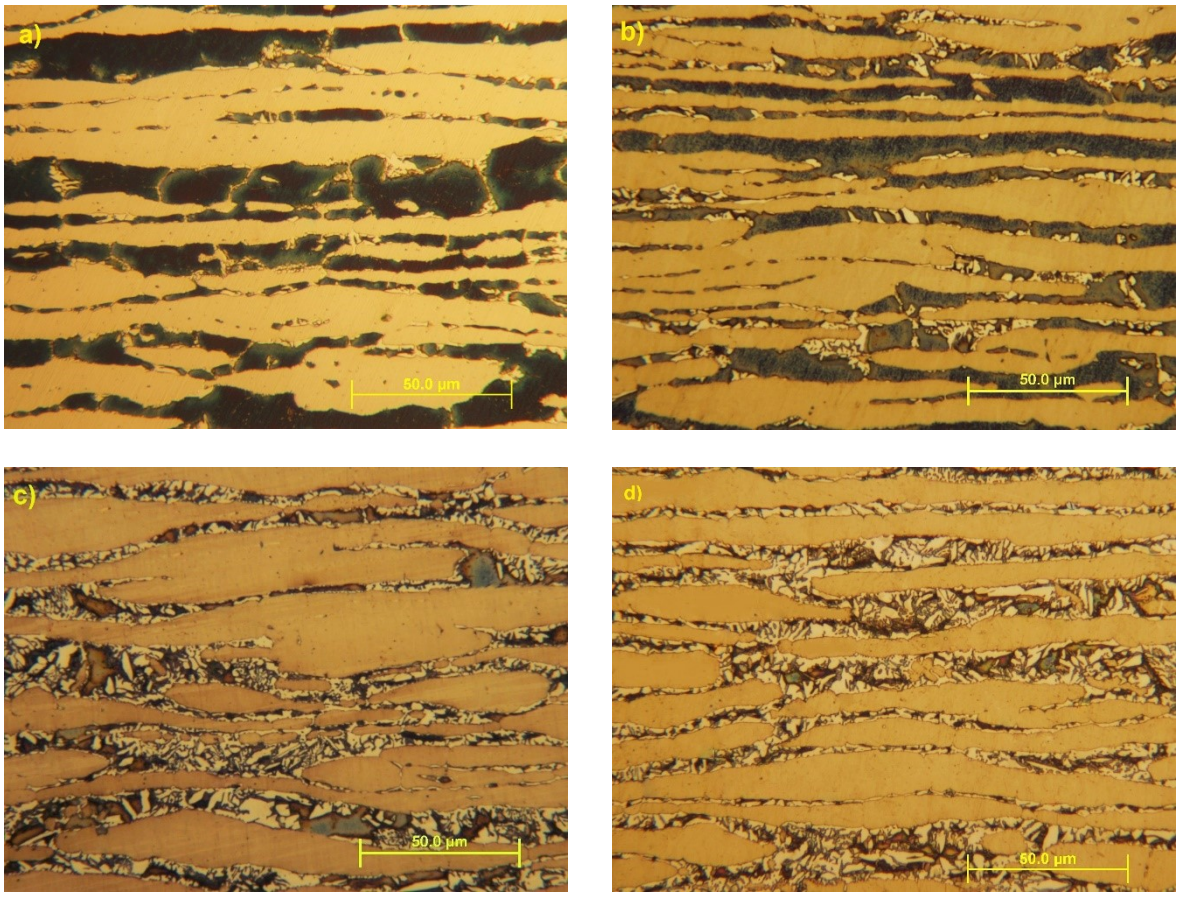

Fig. 16 Microstructure evolution of the samples isothermally aged at T=850°C for different time: a) t=5 min; b) t=15 min; c) t=25 min; d) t=35 min.

To appreciate better the remarkable difference in the decomposition kinetics of Ferrite phase between the two aging temperature, we can observe Fig. 17. It is evident that after 30 min at T=800°C, only few precipitates of σ-phase are grown on the boundaries of ferrite/austenite phases. While at T=850°C, the eutectic decomposition of ferrite is almost concluded.
This results are in agreement with the TTT diagram, because the treatment at T=850°C, being closer to the “nose” of the precipitation curve, is more critical that the one at T=800°C [19].

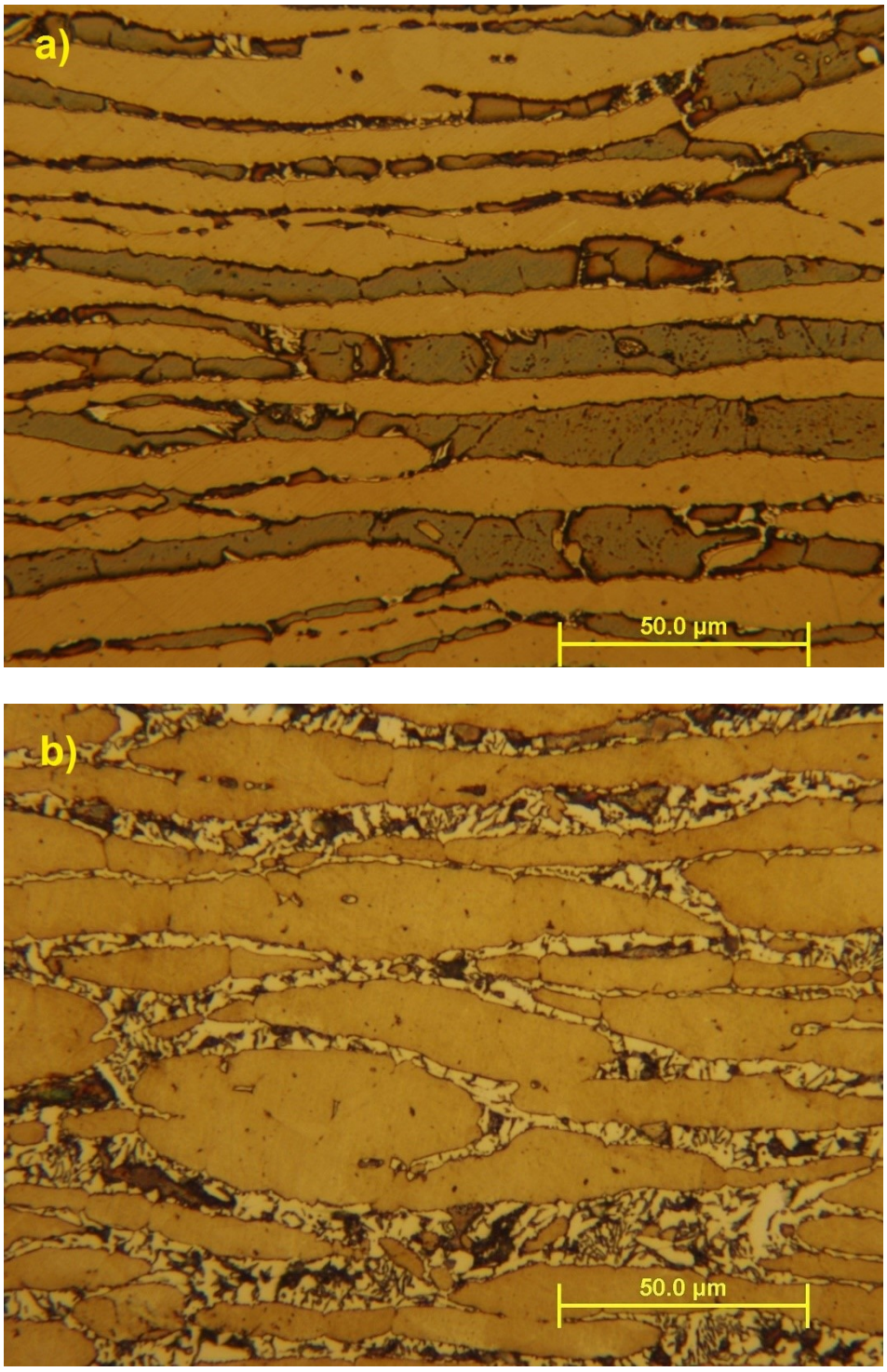

Fig. 17 Microstructure of the samples isothermally aged for t=30 min at different temperature: a) T=800°c; b) T=850°C.

2.3.2. HARDNESS

The results obtained in the hardness test and reported in Fig. 18, are in good accordance with the microstructure evolution observed during the OM analysis. For both the temperature of heat treatment, it can be seen that the hardness of the samples generally increases with increasing aging time. This tendency is due to the increment of σ-phase previously shown. σ-phase is a hard and brittle precipitation, with an hardness of 68 HCr (~940 HV). Therefore, an accretion of this phase causes a remarkable increment of the hardness of the samples.

Even if the general tendency is the same, the way the hardness increases in the two series of samples is quite different.

For the samples isothermally treated at T=800°C, the hardness remains close to the basic value (262 HV) until an aging time of 30 minutes. After this point, the samples experienced a remarkable hardness increase. This happens because, in accordance with the OM analysis, the first precipitate of σ-phase starts to appear on the boundary of the grains only after 30 min.

A different behaviour can be observed in the samples isothermally treated at T=850°C. For those specimens the hardness starts to increase immediately, because of the σ-phase precipitation start already after 5 min of aging treatment. The increment continues until t=30min, and then it settles at a maximum value of 370 HV. The increment stops because at this point all the ferrite phase is decomposed.

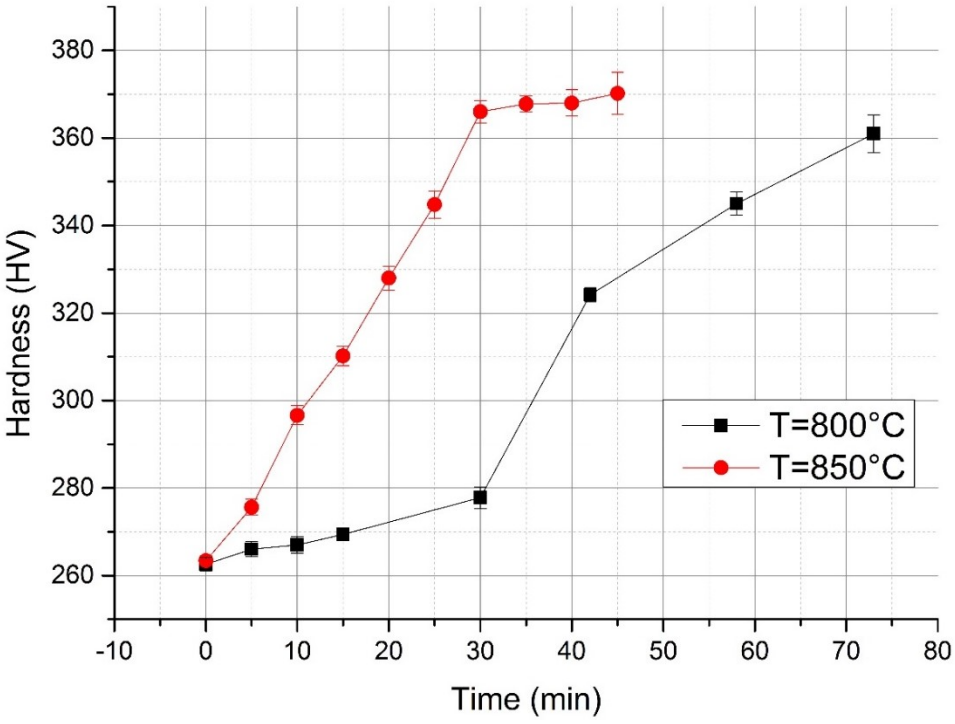

Fig. 18 Change of the hardness as a function of aging time

2.3.3. Stäblein-Steinitz test

In Fig.19 and Fig.20 we reported the values of magnetic saturation (B_s) and Coercivity (H_c), acquired from the hysteresis loops of each sample. The values are plotted against the aging time.

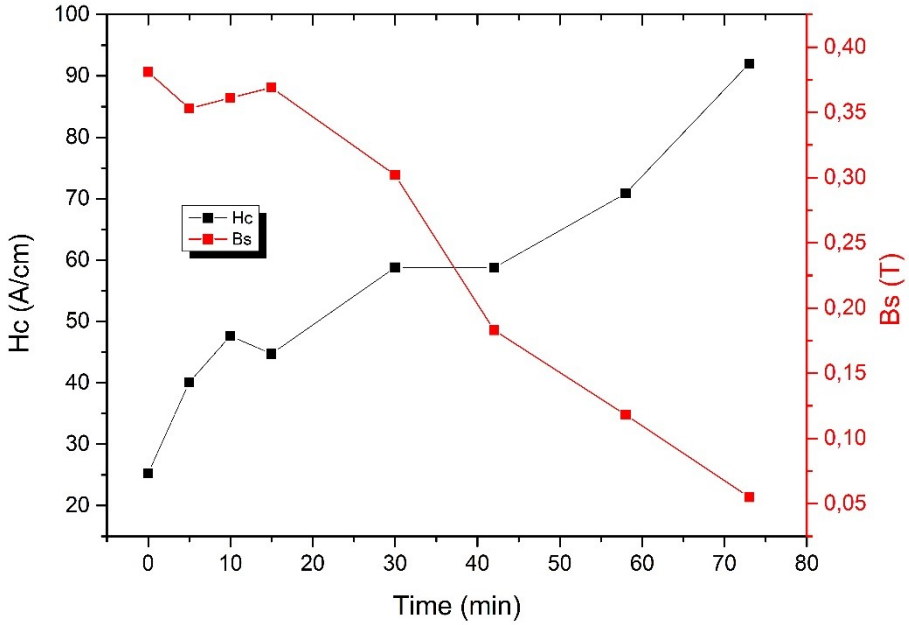

Fig. 19 The change in magnetic saturation (Bs) and coercivity (Hc) with the aging time, for T=800°C

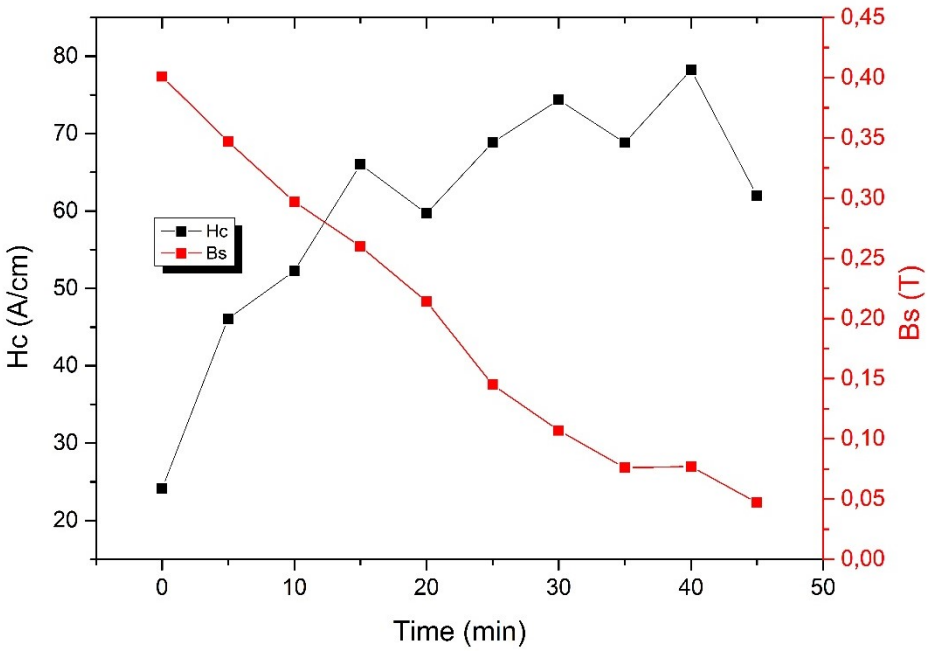

Fig. 20 The change in magnetic saturation (Bs) and coercivity (Hc) with the aging time, for T=850°C

For both the heat treatments, Magnetic saturation (Bs) evidently decreases with increasing aging time. The saturation induction value is known to be proportional to the relative amount of ferromagnetic phase [19] [28].
The tendency of the coercivity is the opposite: increasing the aging time brings to an increment of the coercive force. This result indicates that the dislocation density of α-ferrite grains increased. Therefore, the eutectic decomposition that initially starts on the boundaries, must necessary takes place also inside the ferrite grains during the rest of treatments [28].
Using the proportionality between Bs and the ferromagnetic phase, and knowing the Ferrite content of the base material from the supplier (46,9% of ferrite), we found the Ferrite volume fraction for both the series of samples as a function of the aging time (Fig. 21). The results are clearly in agreement with the one obtained from the OM analysis and the Vickers hardness test. The eutectic decomposition of the ferrite phase in the samples heat-treated at T=850°C appeared for an aging time that is remarkably shorter than the one needed with the lower temperature. In particular, considering the qualitative comparison made in Fig. 18, after 30 minutes of treatment the ferrite content of the sample treated at T=850°C is 12,5%, while in the sample treated at T=800°C is still 37,2%.

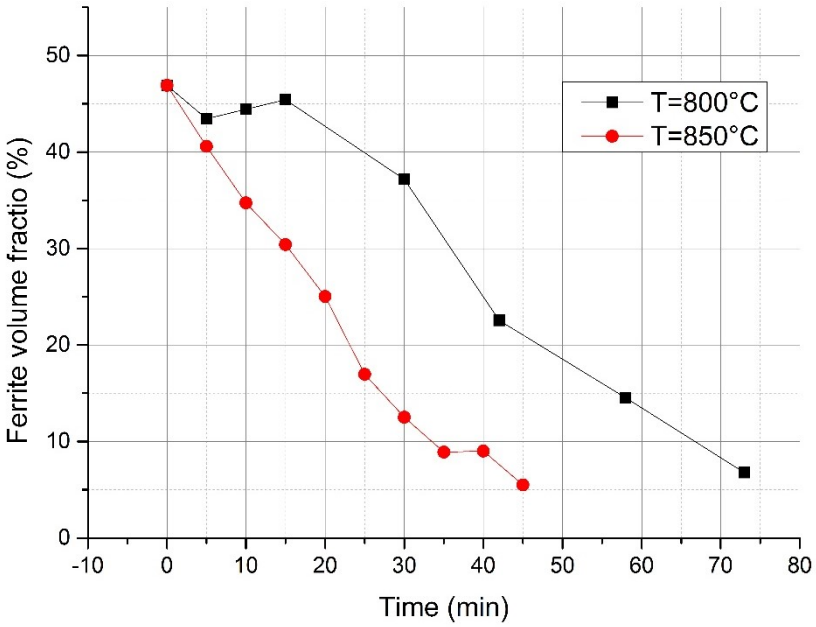

Fig. 21 Dependence of the ferrite content on the aging time of the heat treatments

The kinetics of precipitation of the σ-phase in stainless steels has been described in numerous studies using both analytical and experimental methods. It is well known that the correct quantitative evaluation of σ-phase must be done using EBDS or XDR measurements. During this work, unfortunately these instruments were not available. Nevertheless, according to several studies [19], [24] during eutectic decomposition we can obtain with good approximation the σ-phase fraction from the ferrite decomposition values. There is not a common model for illustrating the kinetics of σ-phase precipitation.

In this work we decided to use the Johnson-Mehl-Avrami equation to describe this process. The JMA equation describes how solids transform from one phase to another at constant temperature. Therefore, it is suitable for our purpose.
The JMA equation is reported below:

$$y = 1 - e^{-kt^n}$$

where y is the transformed volume fraction, t is the aging time, k and n are the Avrami constant. The equation has been used to fit the experimental results of ferrite transformation obtained from the Stäblein-Steinitz test. The fitting curves and the Avrami constants values are reported respectively in Fig. 22 and Table 6. It is clear from Fig 22 that the kinetics decomposition of ferrite phase in SDSS 2507 follows the JAM equation in a satisfactory way.

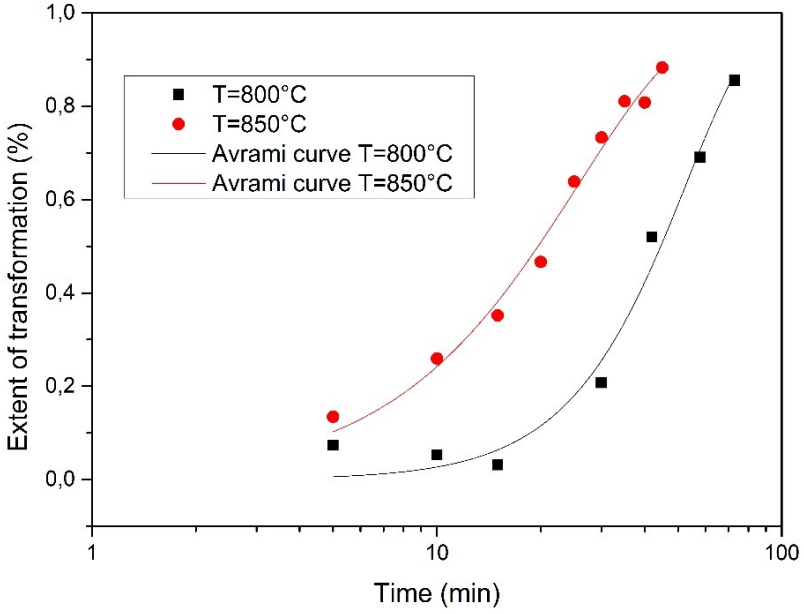

Fig. 22 σ-phase precipitation as a function of aging time

Table 6 The best-fit values of JMA constants for the ferrite phase decomposition

	n	***k***	***t (y=0.5)***
Avrami curve T=800°C	2,16653	1,858 x 10^{-4}	44,53
Avrami curve T=850°C	1,35973	1,21 x 10^{-2}	19,63

There is no clear physical interpretation of the Avrami constants k and n. The JMA constant n is mainly related to different types of nucleation and growth conditions, and it gives an indication of the kinetics responsible for the transformation [24], [29]. However, the obtained constants' results are in accordance with other results found in literature [5], [13].

2.3.4. FISCHER-FERRITE TEST

The Fischer Ferrite test was done on the same samples used for the previous tests, so only one side for each sample was polished. Three measures were taken for each face of the samples (four sides and two faces) and the average was calculated. In Fig.23 and Fig.24, we reported the results of the Ferrite volume fraction of the samples obtained with the Ferrite scope against the aging time.

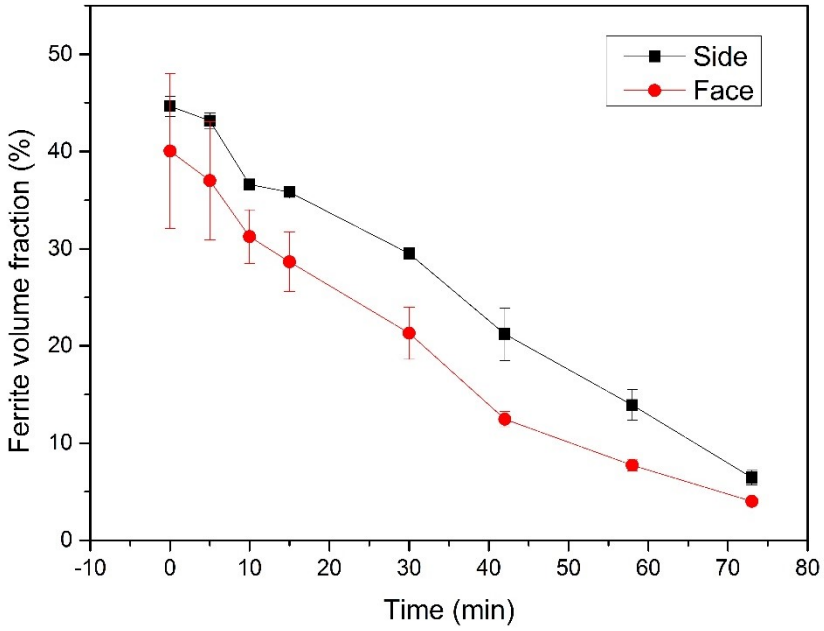

Fig. 23 Dependence of the ferrite content on the aging time of the heat treatment for T=800°C

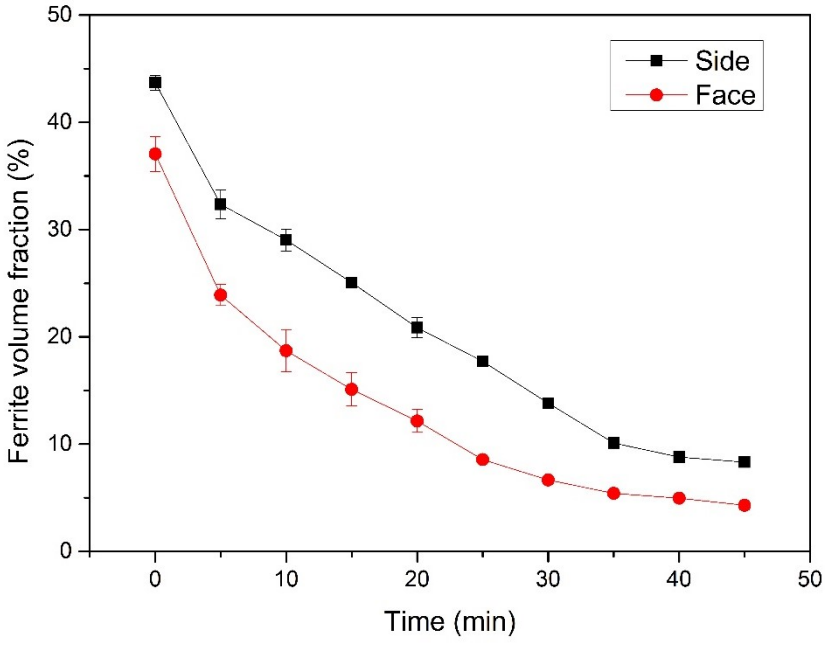

Fig. 24 Dependence of the ferrite content on the aging time of the heat treatment for T=850°C

Results are in good agreement with the one previously obtained with the Stäblein-Steinitz test (Fig.21). The tendency of the ferrite content to decrease with increasing aging time is confirmed.
In our measurements we did not find any difference between the values obtained in the polished side surface, and the ones obtained in the other not-polished sides. However, a difference was found between the sides and the faces. In particular, an increment of the ferrite content was observed from the surface towards the centre of the samples.

CHAPTER 3

EFFECTS OF LASER WELDING ON SAF-2507 SDSS PREVIOUSLY COLD ROLLED

3.1. INTRODUCTION

As pointed out in the previous chapters, the optimum properties of super duplex stainless steels are achieved when nearly equal proportions of ferrite and austenite are present in the microstructure. This balanced ratio between the two phases is obtained with a suitable combination of chemical composition and solution heat treatment. However, during welding processes, because of material melting, the balanced microstructure can undergo detrimental transformations. When SDSS is melted, it solidifies from the liquid phase to a fully ferritic structure. Then, as the material cools down to room temperature, the ferrite transforms into austenite through solid-state transformation [30]. With an improper cooling rate, two main problems may arise: the achievement of an unbalanced austenite-ferrite ratio, and the precipitation of secondary phases in the weld zone (WZ) and heat-affected zone (HAZ) [31]. Both these microstructural changes are highly detrimental for the mechanical and corrosion properties of the SDSS. Therefore, the study of weldability of super duplex stainless steels is a fundamental task for their proper industrial application. Previous investigation demonstrated that conventional welding processes as submerged arc welding (SAW) [32], plasma arc welding (PAW) [33], Gas tungsten arc welding [34], and friction stir welding [35] destroy the balanced ration between the phases, promoting the precipitation of secondary harmful phases. For this reason, in recent years high power laser welding has seen a remarkable increase in research interest, due to its better precision, speed and versatility compared to traditional welding process [36]–[38]. While earlier researchers attempted to study mainly the effect of Laser beam parameters on microstructure and properties of DSS [30], [31], [33], [34], few studied the variation in ferrite-austenite ratio in SDSS welding.

In the present chapter, the effects of Nd: YAG laser welding on microstructure and mechanical/corrosion properties of UNS S32750 (SAF 2507) SDSS samples with seven different grade of deformation (i.e. ε= 0, 10, 20, 30, 40, 50, 60%) have been studied.

3.2. MATERIAL AND EXPERIMENTAL PROCEDURE

3.2.1 MATERIAL AND SAMPLE PREPARATION

The investigated material is the UNS S32750 (SAF2507) SDSS. It was supplied by ARCELORMITTAL. Its chemical composition can be found in Table 7.

Table 7. Chemical composition of SDSS 2507

Element	C	Mn	P	S	Si	Cu	Ni	Cr	Mo	N
%	0.021	0.822	0.0231	0.0004	0.313	0.178	6.592	24.792	3.705	0.2644

The as-received material was a plate of 15 mm thickness, previously solution annealed at 1100°C and water quenched. From this plate material, 14 specimens were cut with the size of 100x15x10 mm for cold rolling.
The samples were deformed in the same direction of the hot rolling, using a double-cylinder mill with a reduction of 0,25 mm at every passage. The maximum deformation was chosen to be 60 %, in order to avoid problems of bending in the samples. The thickness reduction applied in the seven couples of specimens were the following: 0% - 10% - 20% - 30 % - 40% - 50% - 60% (Fig. 25).

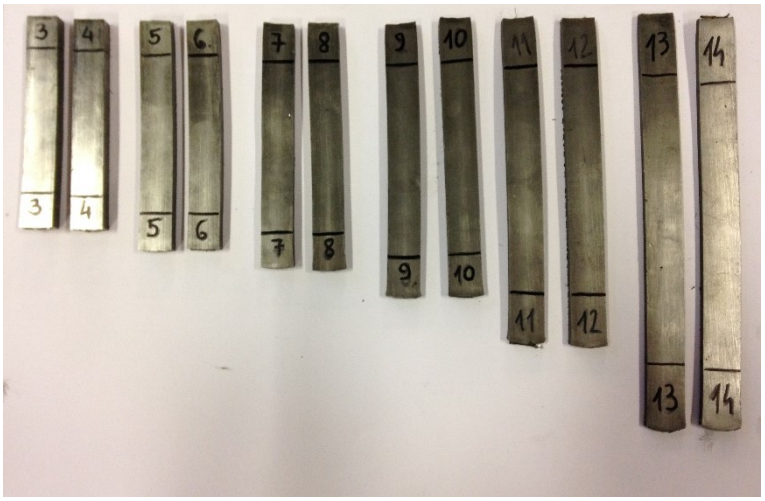

Fig. 25 Couples of samples with different thickness reduction

From the deformed samples, specimens with the size of 70 x 15 x 3 mm were prepared as square butt joints for the laser beam welding.
The welding was performed using a 4KW Rofin-Sinar DY 044 Nd: YAG laser, assisted with a six-axis robot from ABB. The schematic arrangement of laser welding is shown in Fig. 26. For each weld, specimens were fixed on the worktable to prevent distortion during the process. The welding parameters reported in Table 8 were obtained from bead on plate trials experiments, with fixed power and defocusing distance and different welding speed in order to achieve full penetration joints.

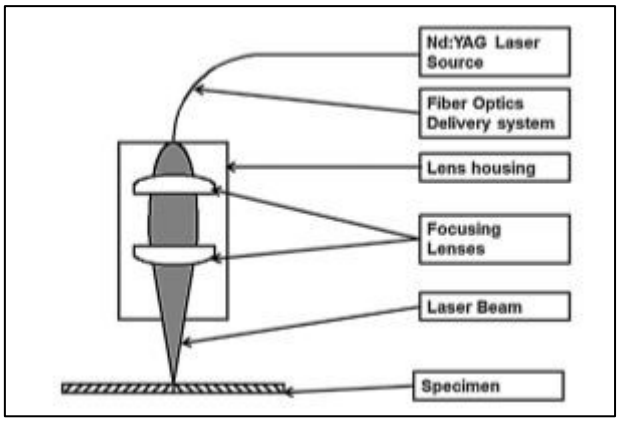

Fig. 26 Schematic of laser welding setup

Table 8 Laser Welding parameters

Parameters	Value	Unit
Average Power	1400	KW
Welding speed	450	mm/min
Defocusing distance	0	mm
Shielding gas/flow rate	Argon/20	l/min

After the welding phase, samples were sectioned transverse to the welding direction for the microstructure examination as well as mechanical and corrosion tests.
The cross section were mounted into epoxy resin, grinded up to 2400 grit paper and polished with clothes (3μ and 1μ) using polycrystalline diamond suspension. Beraha etchant (85ml H_2O - 15ml HCl - 1g K_2S_2O) was used to highlight the microstructure. In Fig. 27, the final result is shown.

Fig. 27 Top and cross surfaces of the sample after the metallographic preparation

3.2.2 OM ANALYSIS

The microstructures of base material (BM), Heat affected zone (HAZ) and weld zone (WM) were examined in the cross and top surfaces of the welded samples (Fig. 27). The OM analysis was carried out with the OLYMPUS PMG 3 microscope, in five different magnification (25x – 100x – 200x – 500x – 1000x). Pictures were taken for every sample.

3.2.3 MICRO HARDNESS TEST

Micro hardness tests were performed in the cross surfaces of the welded samples following the ASTM E384 standard. For the tests, we used a BUEHLERR IndentaMet™ 1105, with a load of 300 grams and an application time of 11 seconds. The extended technical procedure of the hardness test is reported in Chapter 2.2.3. For each sample, four measurements were taken along the midline of the thickness, in the weld zone and in the base material. The measurements of the HAZ were taken along the fusion line because its narrow width did not allow more than one measure in the same quota.

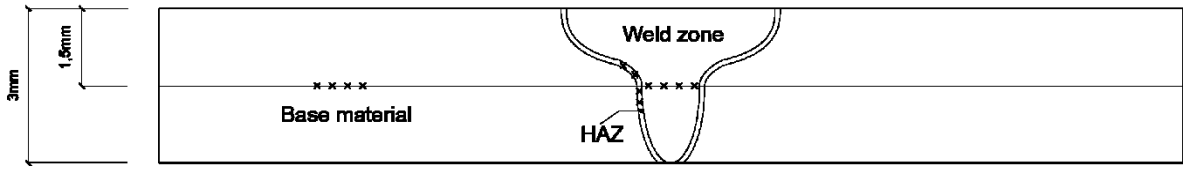

Fig. 28: Schematic of Microhardness test measurement.

3.2.4 EDDY CURRENT TEST

Eddy-current testing (ECT) is a non-destructive electromagnetic test method, which uses electromagnetic induction to detect and characterize surface and sub-surface flaws, as well as ferromagnetic phase content in conductive materials.
The operating principle can be observed in Fig. 29. In an eddy current probe, a coil of conductive wire is excited with an alternating electrical current. This current produces an alternating magnetic field around the coil, which oscillates at the same frequency as the current. If the probe and its magnetic field are placed close to a conductive material, like our SDSS, a circular flow of electrons, known as an eddy current, will begin to move through the metal.
That eddy current flowing through the metal will in turn generate its own magnetic field, which will interact with the coil and its field through mutual inductance. Changes in metal thickness or defects like near-surface cracking will interrupt or alter the amplitude and pattern of the eddy current and the resulting magnetic field.

This in turn affects the movement of electrons in the coil by varying its electrical impedance [13]. With the use of a software, changes in the impedance amplitude and phase angle can be plotted. These results can be used to identify changes in the tested sample.

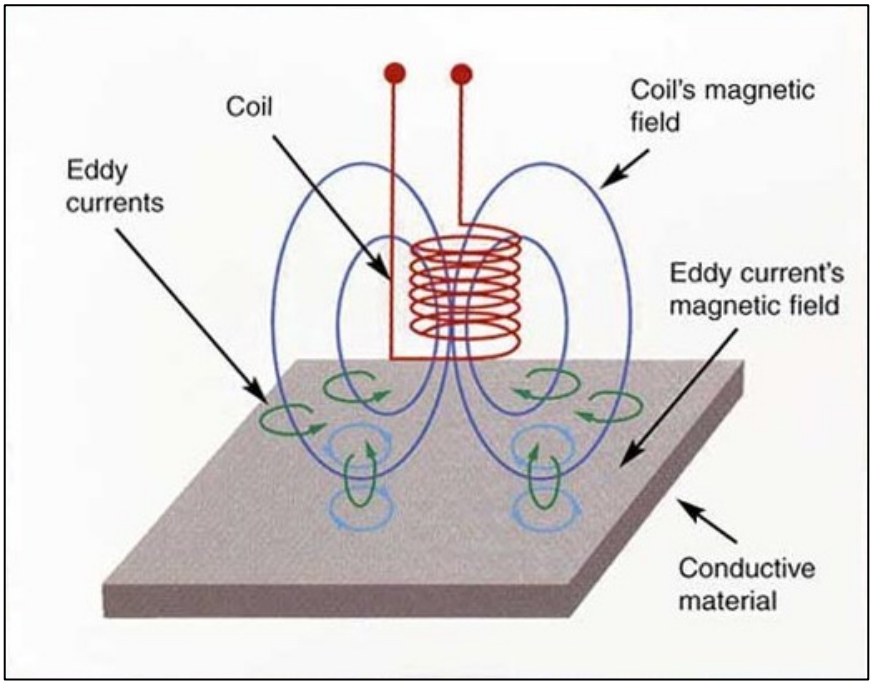

Fig. 29 Eddy-current operating principle

For our test, 13 measurements were made in the top section of each sample, starting from the middle of the joint. The distance between each detection point was 1 mm. The inspection was done in 4 different frequencies: 10,0 KHz – 40,0 KHz – 66,7 KHz – 100,0 KHz. The data acquisition, processing and the control of the set-up were done using a personal computer with “ScanMax” software.

3.2.5 CORROSION TEST

Finally, a corrosion tests was performed following the ASTM G48 for evaluating the pitting resistance of the welded samples. The corrosion test consisted in the total immersion of the samples in a Ferric Chloride Solution for 72 hours at a constant temperature of 50 ± 2°C. The solution was obtained dissolving 100 grams of reagent grade ferric chloride, $FeCl_3 \cdot 6H_2O$, in 900 ml of distilled water (about 6 % $FeCl_3$ by weight). Before the tests, all the sections obtained during the preparation were deburred, washed, dipped in acetone and air-dried. After that, they were weighted in order to measure the material loss after the test and thus calculate the corrosion rate. To increase the amount of surface in contact with the solution, before the cleaning procedure, the samples were drilled in the base material. This allowed us to hang them with a wire to the top of the container. With this procedure the specimens were not in contact with any part of the glass jars. (Fig.30). For the heating, an electric furnace was used.

Fig. 30 Glass container test with the 40% deformed sample totally immersed in the Ferric Chloride Solution

3.3. RESULTS

3.3.1. OM ANALYSIS

The microstructure of the UNS S32750 (SAF 2507) SDSS base material used in the welding experiments is shown in Fig.31. The picture displays a biphasic structure with approximately equal volumes of both ferrite and austenite phases. The grains are strongly orientated along the direction of rolling.

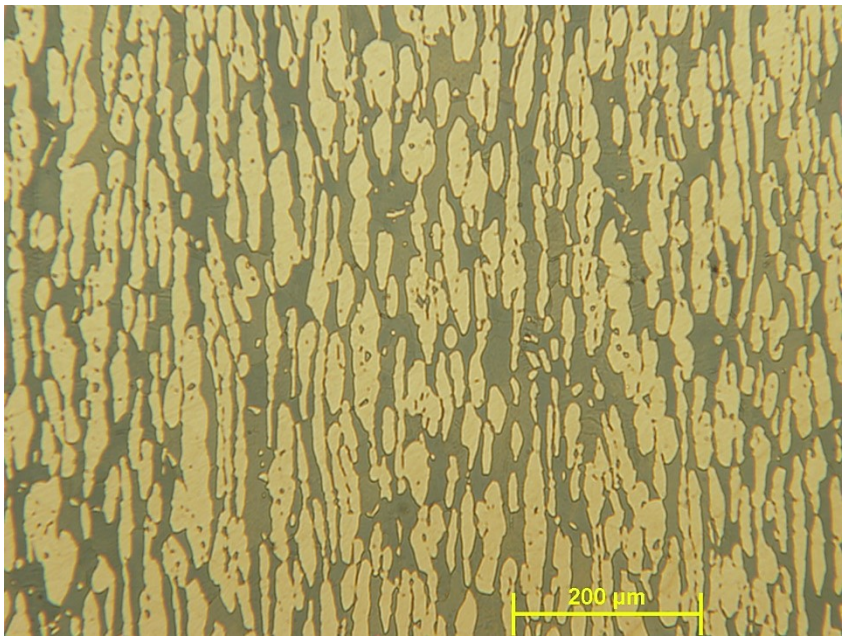

Fig. 31 Base material of the 30% deformed sample

The weld bead observed in the cross section (Fig. 32.a) showed a peculiarity of laser beam welding, where the development of the weld is essentially symmetrical about the axis of the laser beam [31]. In Fig. 32.a and 32.b, the orientation of the grains towards the direction of the heat flux is clear. This is due to the high cooling rate, that in laser beam welding was estimated to be around 1000°C/s [31] [35], [36]. Because of this remarkable cooling rate, the HAZ (Fig. 33.b) was almost undetectable. The fusion line is continuous and clear, with the ferritic grains emanated from the base material grains. In agreement with the CCT diagram relative to σ -phase precipitation for a SAF 2507 [35], no precipitates were observed in this zone during the examination. As previously mentioned, the weld zone initially solidifies into a full ferritic structure, and later partially transforms into austenite through solid-state transformation. Because of the high cooling rate of laser welding, this transformation tends to be inhibited, resulting in a strongly unbalanced microstructure mostly consisting of ferritic phase [30-34] [36]. It is clear in Fig. 33.a that the weld zone is mainly composed of ferrite grains as massive particles, with a low percentage of austenite phase that grew both at ferrite grain boundaries and within the grains. No visible effects were observed due to the different plastic deformation of the welding samples.

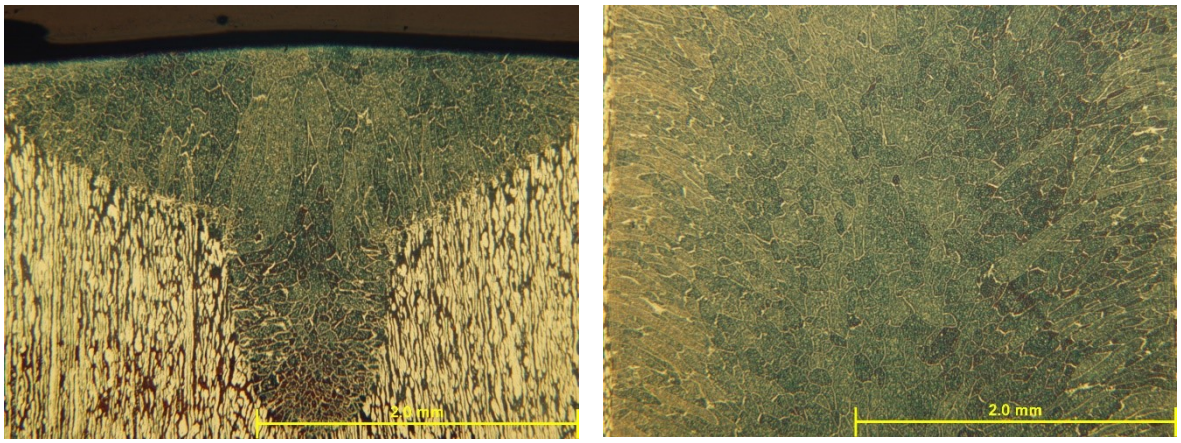

Fig. 32: Cross section (a) and Top section (b) of the weld zone microstructure of the 30% deformed sample at 25x magnification.

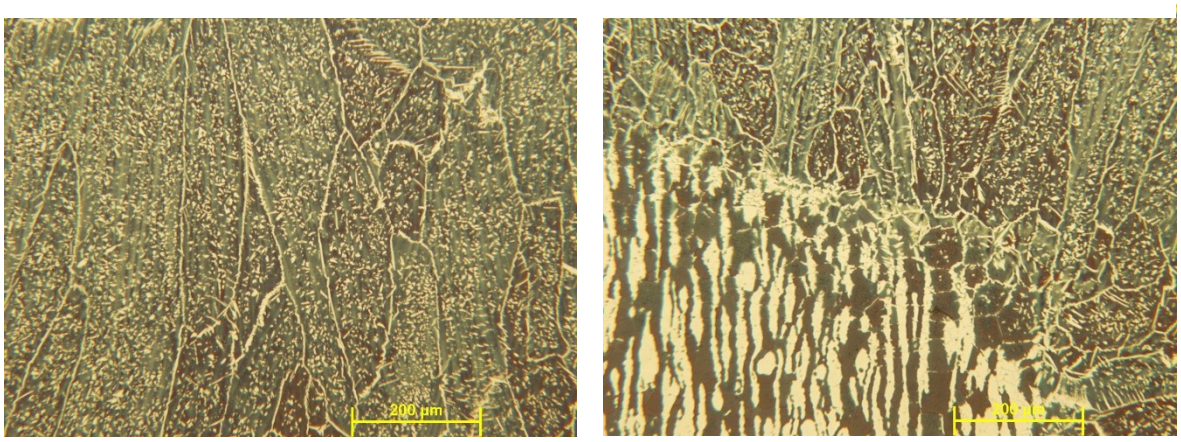

Fig. 33: Weld zone (a) and Heat affected zone (b) of the 30% deformed sample at 100x magnification.

3.3.2. MICROHARDNESS TEST

The Microhardness test results for weld zone (WZ), heat affected zone (HAZ) and base material (BM) are showed in Fig. 34. Provided values are averaged from four readings. In agreement with other studies [37], [39], [40], is clear from the figure that hardness in base material tends to increase with increasing percentage of plastic deformation. This behaviour is due to the interaction between the new dislocations created by the deformation. A different behaviour was observed in the joints. As can be seen from the graphic, the final hardness in the weld zone is ~ 300 HV for all the samples. Because the material in the joint is melted during the welding, the previous deformation has no influence in the final hardness of this zone. Similary, the Hardness in the heat affected zone is not influenced by the percentage of reduction, with an average value ~ 290 HV.
In the case of the non-deformed sample, from the base material (267,5 HV) to the weld zone, an increasing of hardness was observed. This trend is a consequence of the higher amount of ferritic phase discovered in the microstructure of the weld zone compared to the base material (Fig. 33.a). It is well known that the hardness of the bcc phase is higher than the fcc one. Therefore, an unbalanced microstructure rich of ferrite is harder than the starting microstructure.

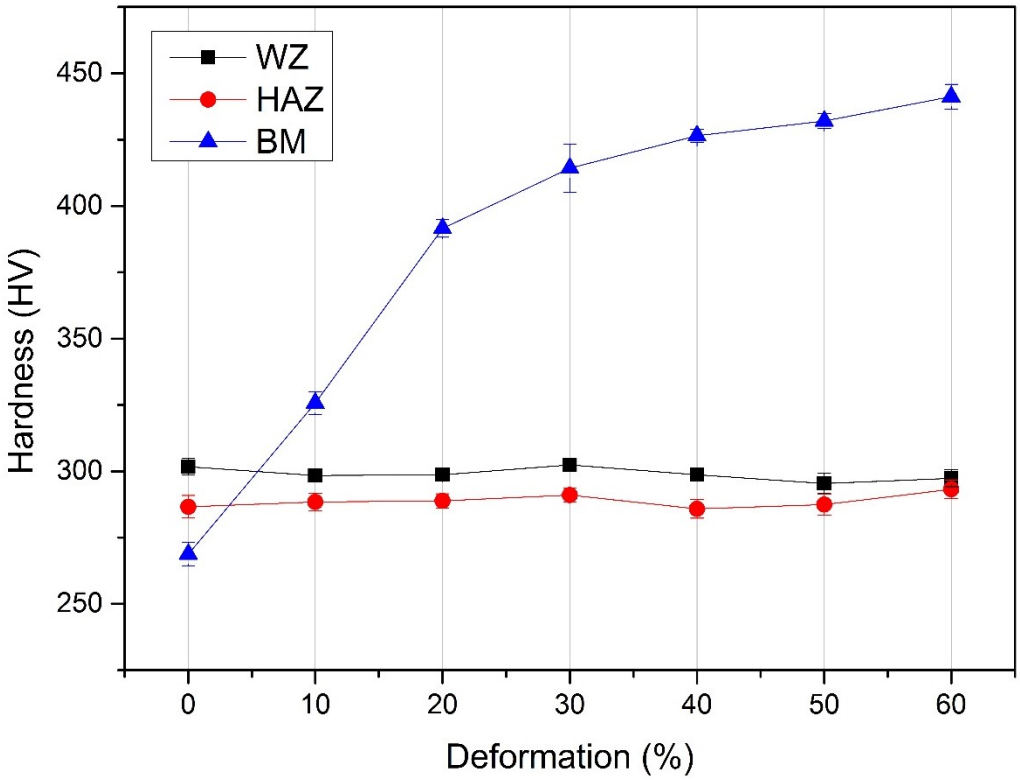

Fig. 34 Change of the hardness as function of the deformation

3.3.3. EDDY CURRENT TEST

The eddy current results for the four frequencies used in the eddy current measurements (10 kHz – 40 kHz – 66,7 kHz – 100 kHz) are reported in the following graphics.

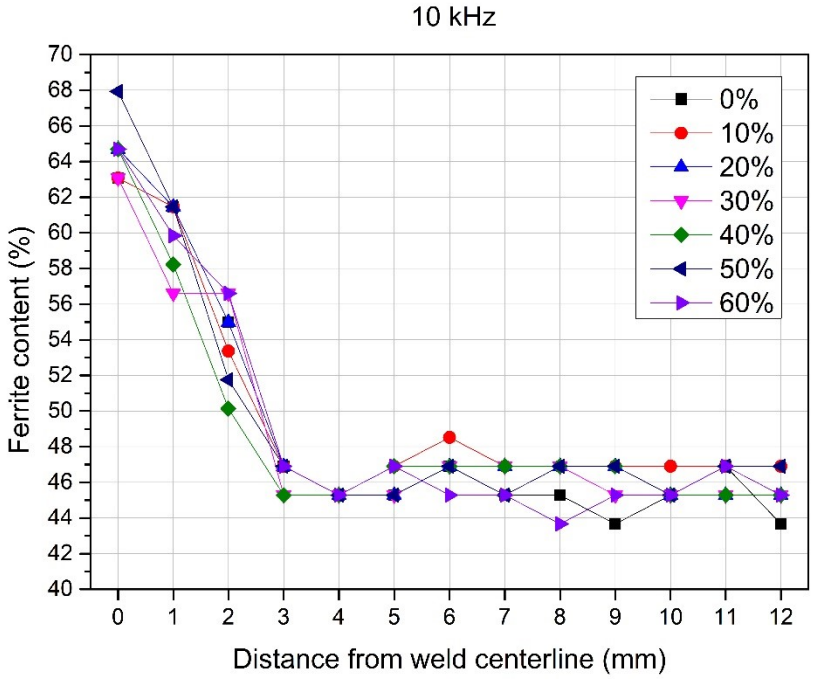

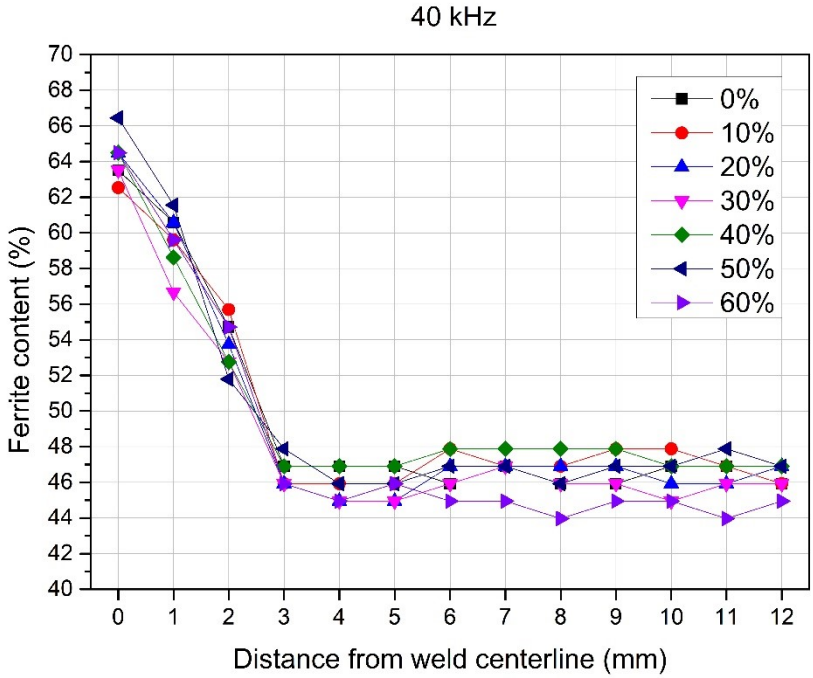

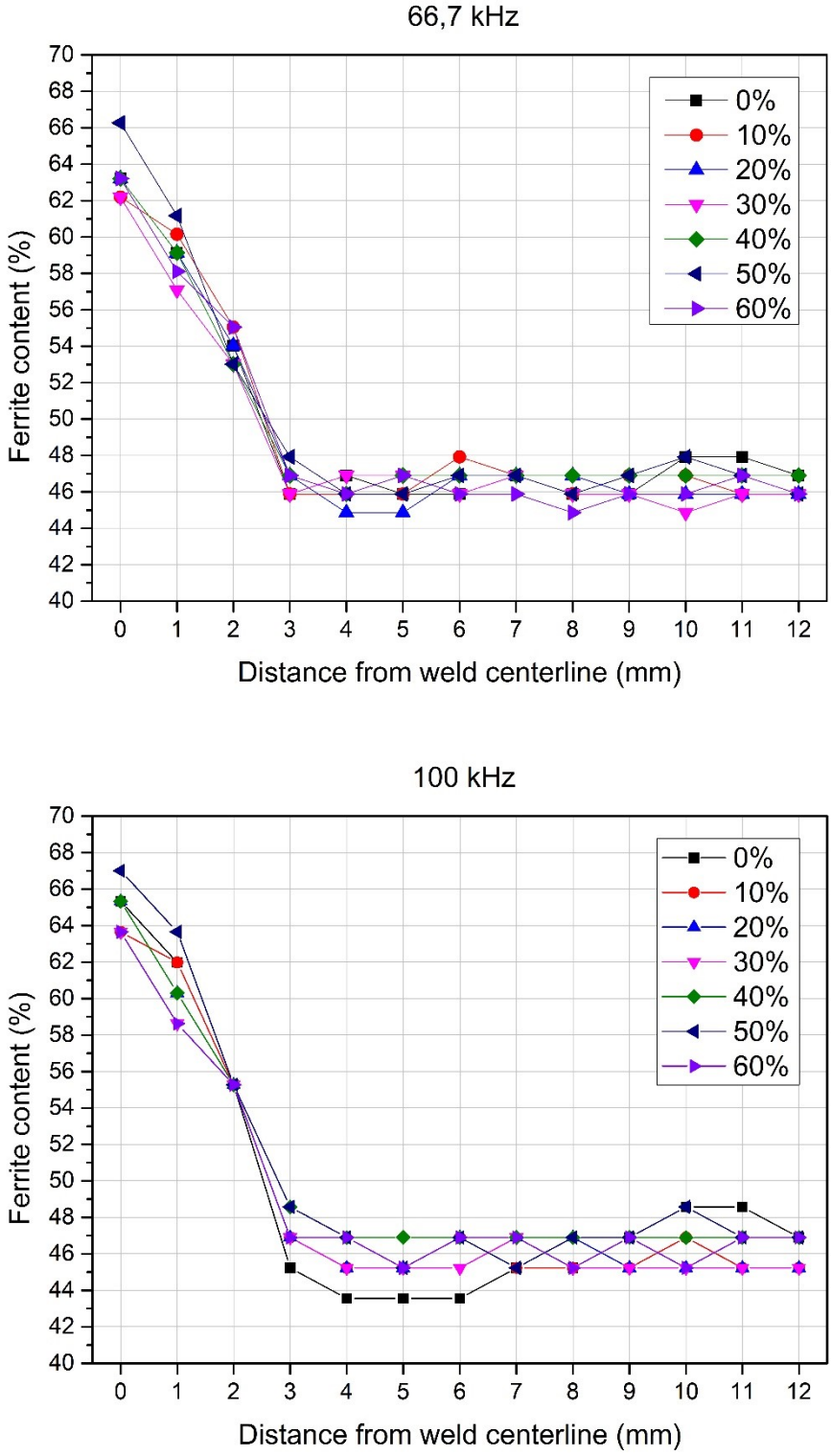

Fig. 35 Ferrite content as function of the distance from the weld centreline measured at four different frequencies

The graphics show the variation of ferrite content measured in the top section of seven different welded samples. As observed during the OM analysis, while looking at the results, it is clear that the previous plastic deformation do not influence the

amount of ferritic phase in both the Weld and the Heat affected zone. In accordance with previous studies [30]–[34], it can be seen that the amount of ferrite in the joint (~64%), due to the high cooling rate typical of the laser welding, is remarkably higher than the one in the base material (46,9%). The precise ferrite content in the HAZ could not be measured because the dimension of the eddy current probe was significantly bigger than the dimension of the zone (~50 μm). However, the tendency of the Ferrite content to decrease with increasing distances from the middle of the joint is quite clear for every frequency. During the test, we observed that the 40 kHz frequency was the most sensitive to the ferrite content variation.

3.3.4. CORROSION TEST

The results of corrosions tests done in laser butt welded joints are shown in table 9.

Table 9 Mass reduction results for the welded samples

Sample	Deformation (%)	Mass reduction after 72h (%)	Corrosion rate (g/cm^2)
1/2	0	5,54	0,03
3/4	10	6,66	0,03
5/6	20	7,11	0,03
7/8	30	6,85	0,03
9/10	40	6,40	0,03
11/12	50	6,64	0,03
13/14	60	5,99	0,03

Results suggest that different plastic deformations did not influence the corrosion resistance of the welded samples. This is in agreement with the previous results, because no significant differences were found between samples microstructure. It is well known that the corrosion rate in duplex stainless steels is enhanced both by the presence of precipitates and by an unbalanced austenite/ferrite ratio. For this reason, a strong corrosion was observed in the weld zone of all the samples (Fig.36), where the ferrite content was found to be ~64%. The joints are highly damaged, and the pitting holes can be observed by the naked eye.

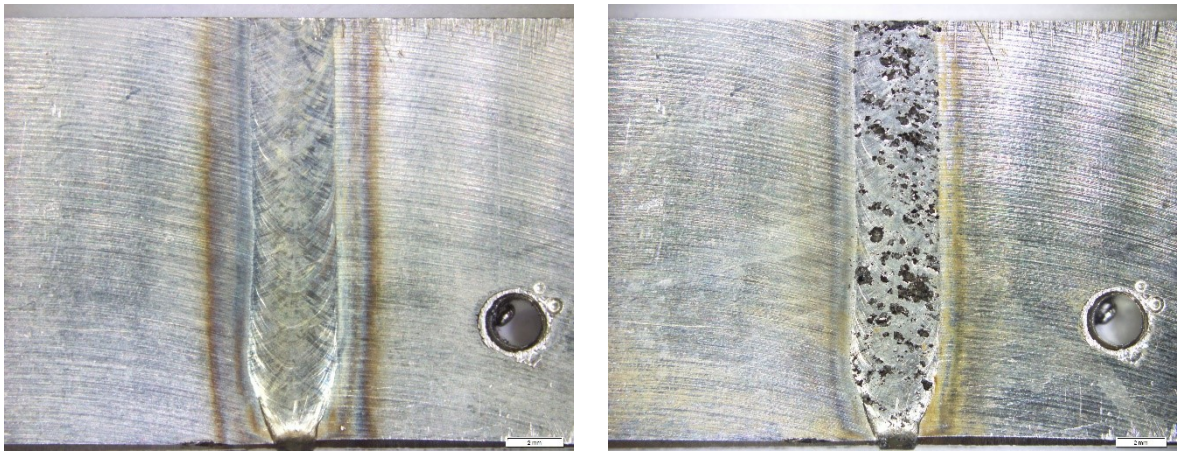

Fig. 36 Top surface of sample with 30% of plastic deformation pre and post corrosion test

As explained in the procedure chapter 3.2.5, the corrosion resistance evaluation is based only on the weight loss measure. For this reason, because of the slight variations of mass measured during the test, it hit can give only qualitative indication about corrosion rate. For a reliable quantitative measurement of corrosion resistance, polarization techniques and CPT measurements must be used, in order to obtain detailed information on active/passive behaviour and different critical pitting temperatures. These tests are planned in a running project.

CHAPTER 4
EFFECTS OF NITROGEN-CONTANING BACKING GAS ON MICROSTRUCTURE AND CORROSION RESISTANCE OF LDX 2101 AND LDX 2404

4.1. INTRODUCTION

In the previous chapter, the detrimental effects of an unbalanced austenite/ferrite ratio in the weld zone have been described. The chemical composition of the weld metal is of fundamental importance in order to obtain a balanced structure after welding. It is well know that duplex stainless steels solidify as delta ferrite. The ferrite to austenite solid-state transformation, which happens only after solidification, is driven by the atomic nitrogen diffusion. Nitrogen is an interstitial element that strongly promotes austenite formation. From the Nickel equivalent equation, according with the WRC-1992 [41], Nitrogen is 20 times more effective as austenite stabilizer than Nickel. A high content of this element rises the ferrite to austenite transformation temperature and enhance the austenite growth rate [42], [43]. At the same time, it plays a fundamental role in the pitting corrosion resistance of the material. As we know from the equation of PREN (Pitting resistance equivalent number) [44], Nitrogen is 16 times more effective in increasing pitting resistance than Chromium. Nitrogen loss from the weld pool during welding process can cause a remarkable decrease in pitting corrosion resistance, because of the decreased austenite content in the weld metal. It can also bring to a precipitation of chromium nitrides. At the same time, too high austenite fractions can result in increased segregation, with detrimental effects on corrosion resistance as well. For these reason, keeping the chemical composition of the parent metal in the weld zone and in the heat affected zone is crucial. In order to obtain this, Nitrogen can be added to the shielding and backing gases. Various authors have investigated the effects of using nitrogen-content shielding gas on the microstructure and corrosion resistance of duplex stainless steels joints. Westin et al. [44], [45] demonstrated that a mixture of 97% Ar + 3% N_2 as shielding gas, instead of full Argon, significantly enhance the austenite formation and the pitting corrosion resistance of lean duplex joint in process like Gas tungsten arc welding (GTAW) and Nd: YAG laser-GTA welding. Zhang et al. [46] reported the same tendency also for flux-cored arc welding (FCAW) experiments. If the effects of Nitrogen used as shielding gas have been widely studied, few investigations were done about its usage as backing gas. The use of Nitrogen as backing gas is of great interest for industrial applications such as pipe welding. Nitrogen is thriftier compared to Argon. Furthermore, in pipe welding application, the root side is highly exposed to corrosion. Having an unbalanced microstructure in this zone, with both tow high or too low austenite, can bring to a decrease of mechanical properties and corrosion resistance of the material.

For these reasons, the objective of this work was to determine the effect of Nitrogen on the root weld microstructure compared to the traditional full Argon backing gas. The material used in this investigation were the recently developed UNS S32101 (LDX 2101) and UNS S82441 (LDX 2404). Lean Duplex grades like LDX 2101 have successfully replaced the austenite low-alloyed austenitic grades as AISI 304L and AISI 316L, and its industrial applications are in continuous development. Lean duplex grades are obtained replacing Nickel content with high amount of Nitrogen. Therefore, for this family of material it is of fundamental important to balance the Nitrogen content, as Nitrogen is the main austenite promoter and no other alloys in the composition can compensate its loss [41]–[43], [47].

4.2. MATERIAL AND EXPERIMENTAL PROCEDURE

The investigated materials were the LDX 2101® (EN 1.4162, UNS S32101) and the LDX 2404® (EN 1.4662, UNS S82441). They were supplied by OUTOKUMPU. Their nominal composition is reported in Table 10.

Table 10. Chemical composition of LDX 2101 and LDX 2404 given by the supplier.

Base material	C	Mn	Cu	Ni	Cr	Mo	N
2101	0.03	5.0	0.3	1.5	21.5	0.3	0.22
2404	0.02	3.0	0.4	3.6	24.0	1.6	0.27
ER 2209	<0.015	2	/	8.8	22.5	3.2	0.15

The materials were received as annealed plates of 3 mm thickness. From those plates, samples with the size of 50x100x3 mm and 40x100x3 mm were obtained respectively for LDX 2101 and LDX 2404. The specimens were prepared as square butt joints for the welding experiment. The gas metal arc welding (GMAW) was performed with a REHM MegaPuls 300 fed with an Ø1.2 mm Avesta ER 2209 (22 Cr 09 Ni 3 NL) as filler metal. Machine settings are shown in Table 11. The welding torch was fixed to a linear drive machine (Yamaha F1405-500), in order to perform run welds at a constant speed of 10 mm/s. For each weld, specimens were previously cleaned with acetone and then fixed on the worktable, keeping a gap of 1 mm between them. The welding set up is shown in Fig. 37. Three different backing gases were used for each material: 100% Ar, 100% N_2, 95% N_2 + 5% H_2, plus a weld without backing gas. As shielding gas, a mixture of 98% Ar and 2% O_2 was employed for all the welding, which is recommended for welding duplex stainless steel. The presence of the Oxygen as active component is required to stabilize the arc. The flow rate was 9 l/min for the backing and 15 l/min for the shielding gas. The welding parameters registered during the experiments are reported in Table 12.

Table 11 Welding machine chosen settings for the experiments.

Parameter	Value	Unit
Current	138	A
Voltage	19,2	V
Wire feed	4,7	m/min
Shielding flow rate	15	l/min
Backing gas flow rate	9	l/min
Material thickness	3,3	mm
Welding process	Standard pulse mode	

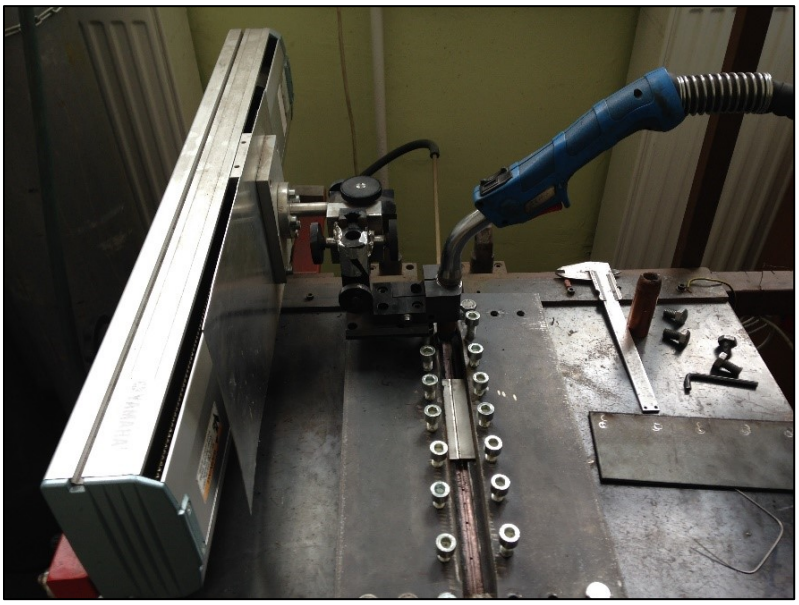

Fig. 37 Schematic of GMA welding setup

Table 12 GMA Welding parameters

Sample	Material	Backing gas	Current [A]	Voltage [V]	$V_{welding}$ [mm/s]	Theoretical Heat Imput* [kJ/mm]
1/1	2101	No	144	21,9	10	0,252
2/1	2101	100% Ar	145	22	10	0,255
3/1	2101	100% N_2	145	21,6	10	0,251
3/2	2101	100% N_2	145	21,4	10	0,248
4/1	2101	95% N_2 + 5% H_2	147	20,7	10	0,243
1/1/2	2101	No	146	21,9	10	0,256
1/2/2	2101	100% Ar	145	21,8	10	0,253
1/3/3	2101	100% N_2	143	22,6	10	0,259
1/4/2	2101	95% N_2 + 5% H_2	144	22,6	10	0,260
2/1/1	2404	No	145	22,1	10	0,256
2/2/1	2404	100% Ar	146	21,7	10	0,253
2/3/1	2404	100% N_2	144	21,8	10	0,251
2/4/1	2404	95% N_2 + 5% H_2	145	21,7	10	0,252
2/1/2	2404	No	145	22,1	10	0,256
2/2/2	2404	100% Ar	144	22	10	0,253
2/3/2	2404	100% N_2	145	22,1	10	0,256
2/4/2	2404	95% N_2 + 5% H_2	145	22,1	10	0,256

**Heat input is theoretical because impulse mode was used in the experiments*

After the welding phase, samples were sectioned transverse to the welding direction for the microstructure examination. The cross sections were put into epoxy resin and grinded up to 2400 grit paper. After they were polished with clothes (3μ and 1μ) using polycrystalline diamond suspension. Beraha etchant (85ml H_2O - 15ml HCl - 1g K_2S_2O) was used to highlight the microstructure. This reagent makes the ferrite dark and the austenite clear. The result is shown in Fig.38.

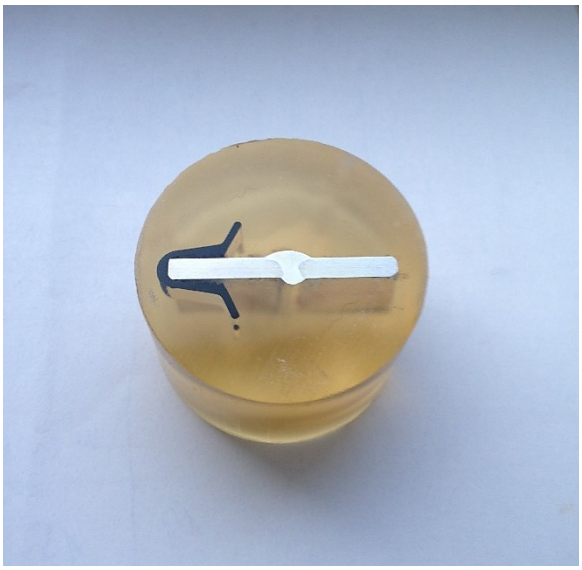

Fig. 38 Sample after the metallographic preparation

The OM analysis of root weld microstructure was carried out in the cross surface of each sample using the OLYMPUS PMG 3 optical microscope, in five different magnifications (25x – 100x – 200x – 500x – 1000x). Ten Pictures of the root zone were taken for every sample at 200x magnification, in order to measure the ferrite content with JMicroVision 1.2.7 image analyser software. The ferrite content was measured also using a Fischer Feritscope FMP30. Ten measurements were taken for each sample along the root weld, with a 5 mm spacing between the detection points. A corrosion test was performed following the ASTM G48 for evaluating the effect of the different backing gases on the pitting resistance of the welded samples. After being cleaned and weighted, the samples were submerged into a Ferric Chloride Solution for 72 hours at a constant temperature of 50 ± 2°C. The samples were weighted again after the test to evaluate the corrosion rate (in g/cm^2). The exposed area of each sample was calculated using a solid modelling software (Solidworks). An Olympus SZX16 stereomicroscope was used to take pictures of the root weld before and after the test, to have a qualitative measure of the corrosion rate.

4.3. RESULTS

4.3.1. OM ANALYSIS

The base material microstructure of both the UNS S32101 (LDX 2101) and UNS S82441 (LDX 2404) is shown in Fig. 39 a) and b). Both pictures display a biphasic microstructure consisting of ferrite and austenite in approximately equal proportions. The grains are strongly orientated along the direction of rolling.

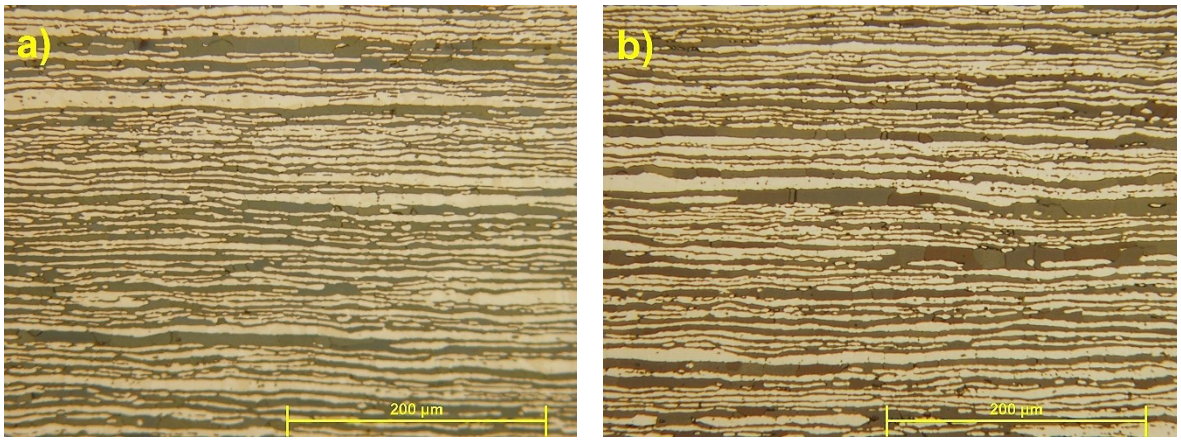

Fig. 39 Microstructure of LDX 2101 (a) and LDX 2404 (b) base material

The root zone microstructure of the LDX2101 and the LDX 2404 for the four different backing gases combination is shown in Fig. 40 and 41.
From the microstructure analysis, in both the material a slight increasing of austenitic phase was observed in the sample with *100% N_2* and *95% N_2 + 5% H_2* as backing gas (Fig.40.c, 40.d and Fig.41.c, 41.d). No remarkable differences were observed between the samples welded without backing gas and with full Argon. The austenitic phase was observed as both grain boundary allotriomorphic austenite and as Widmanstätten side plates. This austenite structure require a relatively small driving force and suggest a relatively slow cooling rate, typical of GMAW welding technique.

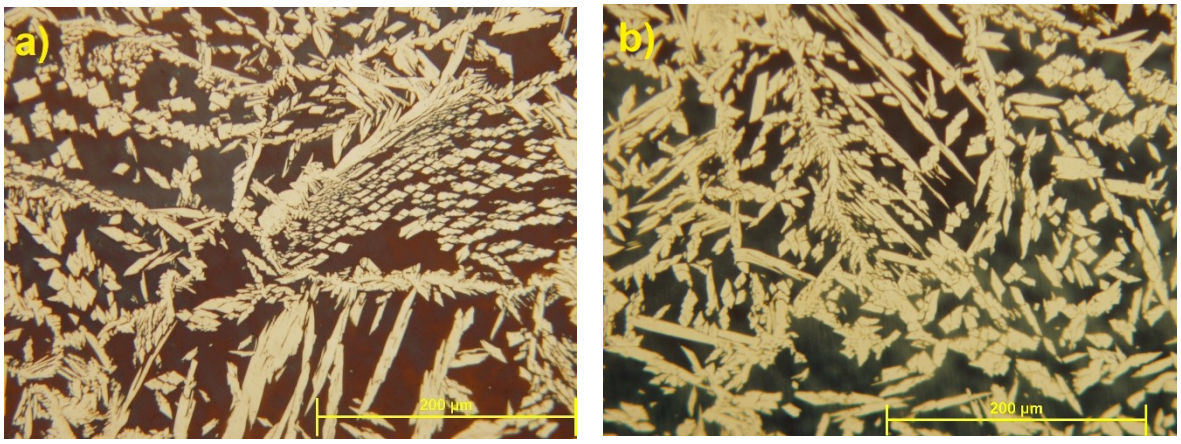

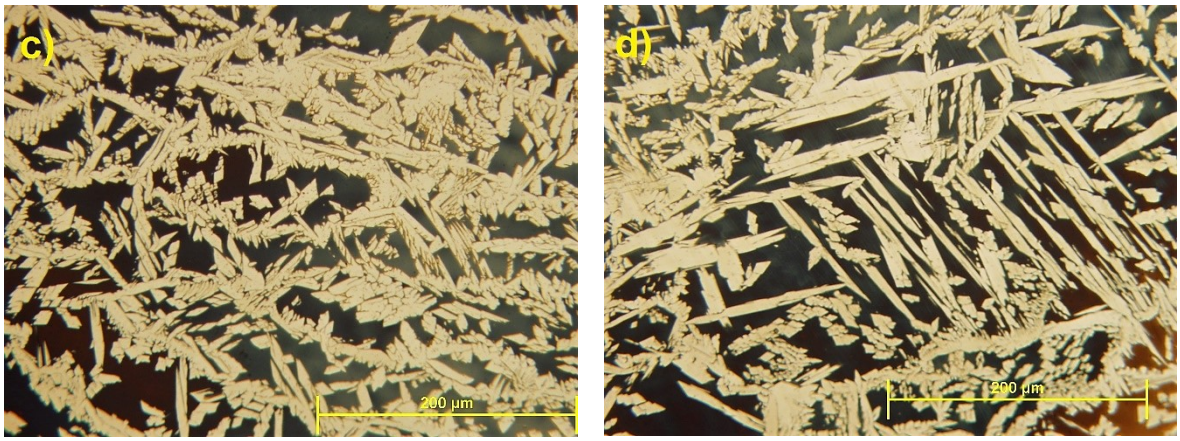

Fig. 41 Root zone microstructure of LDX 2101 for the four different backing gas combination: no backing gas (a), 100% Ar (b), 100% N2 (c), 95% N2 + 5% H2 (d).

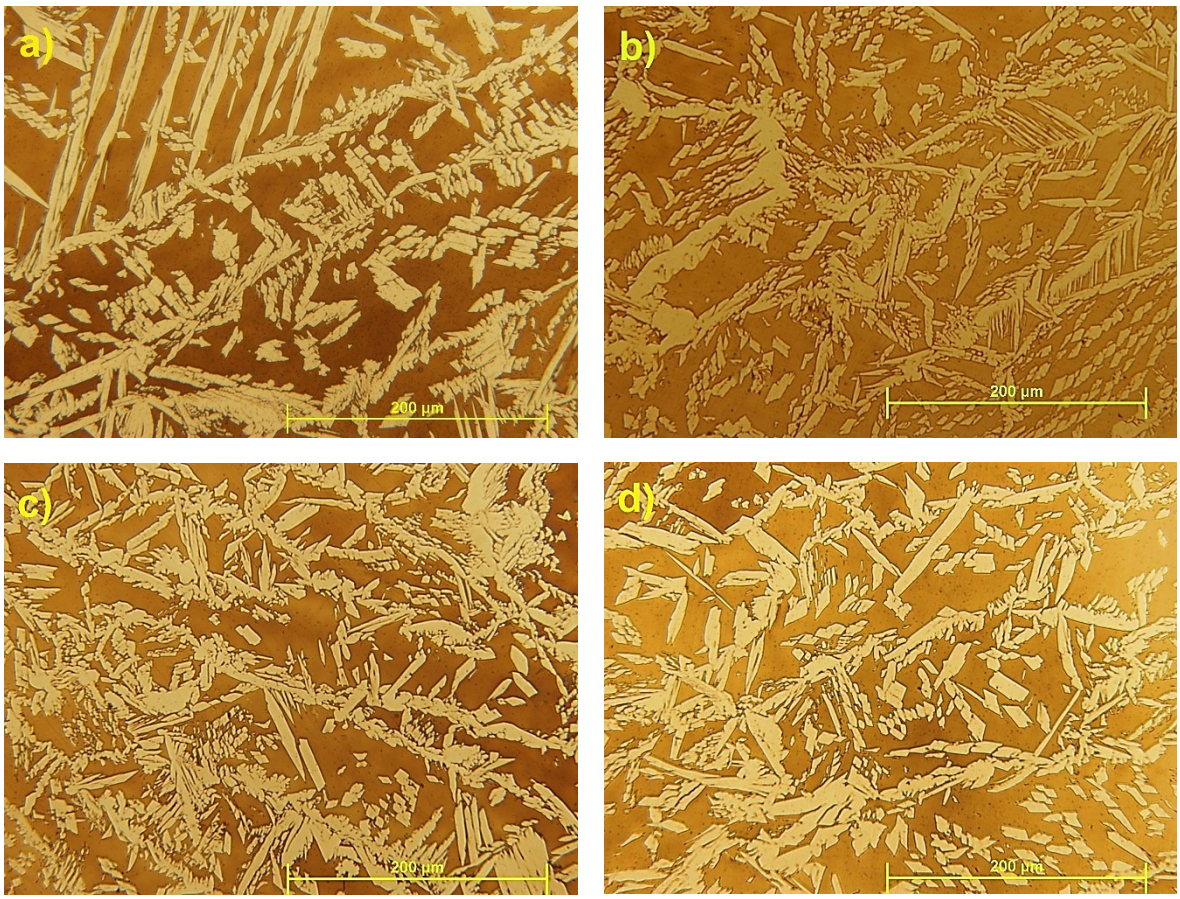

Fig. 40 Root zone microstructure of LDX 2404 for the four different backing gas combination: no backing gas (a), 100% Ar (b), 100% N2 (c), 95% N2 + 5% H2 (d).

4.3.2. FERRITE CONTENT

The ferrite content measured in the root weld of both materials is reported in Fig. 42. Provided values are averaged from ten measurements for both the inspecting methods (Feritscope and Image analyser software).

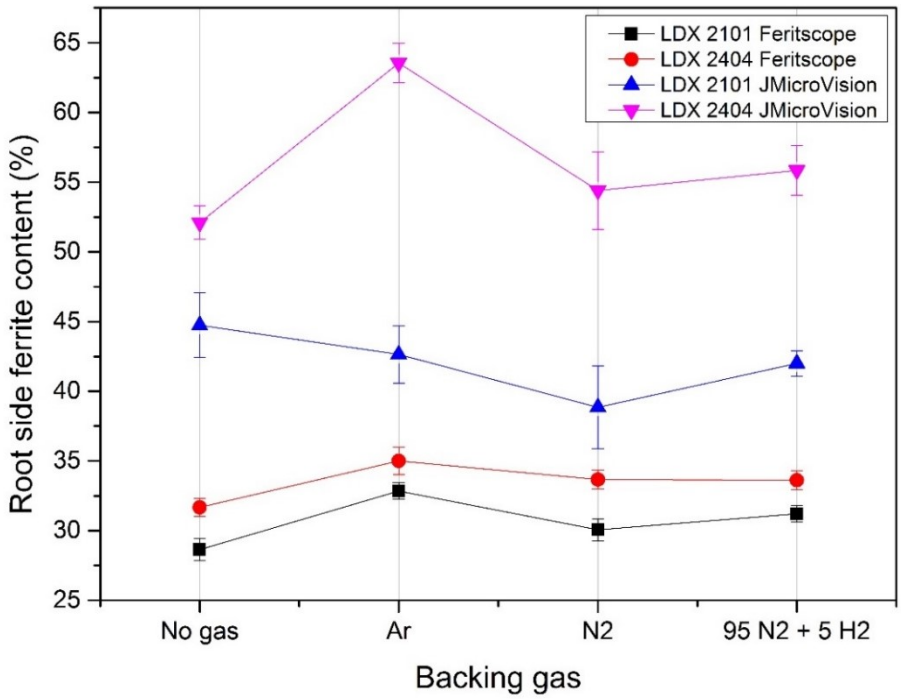

Fig. 42 Root side ferrite content of LDX 2101 and LDX 2404

From the results is quite clear that for samples welded without backing gas, the oxidation compromised a correct measurement of the ferrite content in the root weld. Therefore, those values have been discarded.

The results obtained with the Feritscope are evidently lower than the one measured with the image analyser software. In the Feritscope test, the measurements were taken along the peak of the root weld. Because of the small radius of curvature of the root weld, the scope could not be in full contact with the detected area. The air in contact with the scope resulted in a low ferrite content measurements. In previous study [48], the Feritscope error in root weld measurements was quantify to be around 17%. Therefore, we can consider the results obtained with the image analyser software as the most accurate.

Even if there is a remarkable difference between the two different techniques, a common tendency can be observed. In agreement with the qualitative evaluation performed during the OM analysis, the ferrite content tends to decrease using Nitrogen as Backing gas instead of pure Argon. Being a strong austenite stabilizer, Nitrogen enhances the formation of austenitic phase during solid state transformation. The addition of Hydrogen did not influence the microstructure in a substantial way, but the ferrite slightly increased compared to pure Nitrogen.

4.3.3. CORROSION TEST

The corrosion test results for LDX 2101 are shown in Tab 13.

Table 13 Corrosion test results for LDX 2101

Backing gas	Original mass (g)	Mass after 72h (g)	Mass reduction after 72 h (%)	Corrosion rate (g/cm2)
No gas	15,98	15,13	5,32	0,05
100% Ar	17,33	16,46	5,04	0,05
100% N_2	18,45	17,61	4,55	0,04
100% N_2-2	17,36	16,49	5,02	0,05
95% N_2 + 5% H_2	17,12	16,31	4,72	0,05

For the welded samples having full Nitrogen and *95% N_2 + 5% H_2* as backing gases, a slight decrease in mass reduction was observed compared to the welded sample without backing gas. A smaller improvement was measured for the 100% Ar configuration (Fig 43). These values suggest that nitrogen could have a direct influence in the pitting corrosion resistance also when used as backing gas. Results indicate also that nitrogen can be a proper alternative to the traditional full Argon configuration. In according with Fig. 44, the corrosion in root weld and HAZ was restrained, with some pitting in base material. A test was done also for the configuration with full Nitrogen and a halved flow rate. In this case the corrosion rate

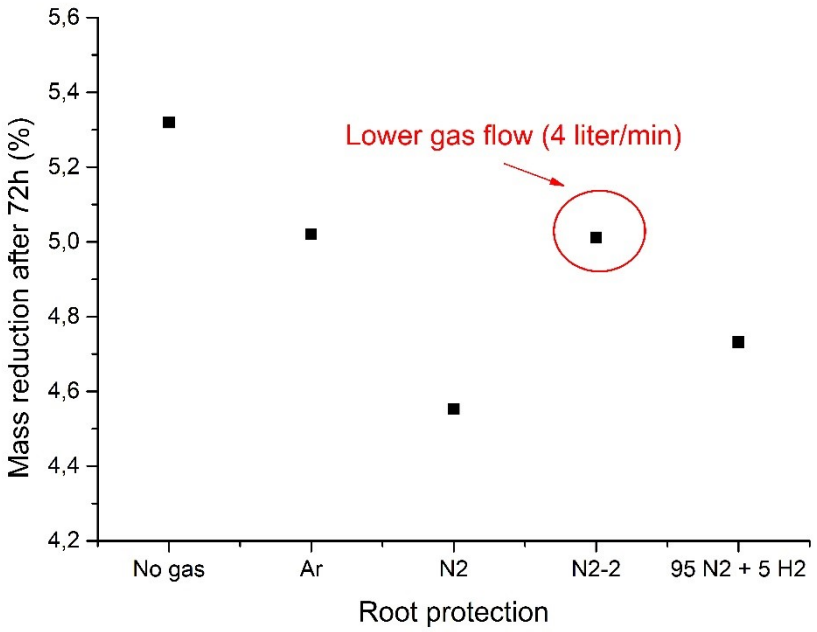

Fig. 43 Values of LDX 2101 mass reduction after 72h (%) relating to the different backing gases

is close with the full Argon configuration. The impact of flow rate in corrosion resistance will be part of a future work.

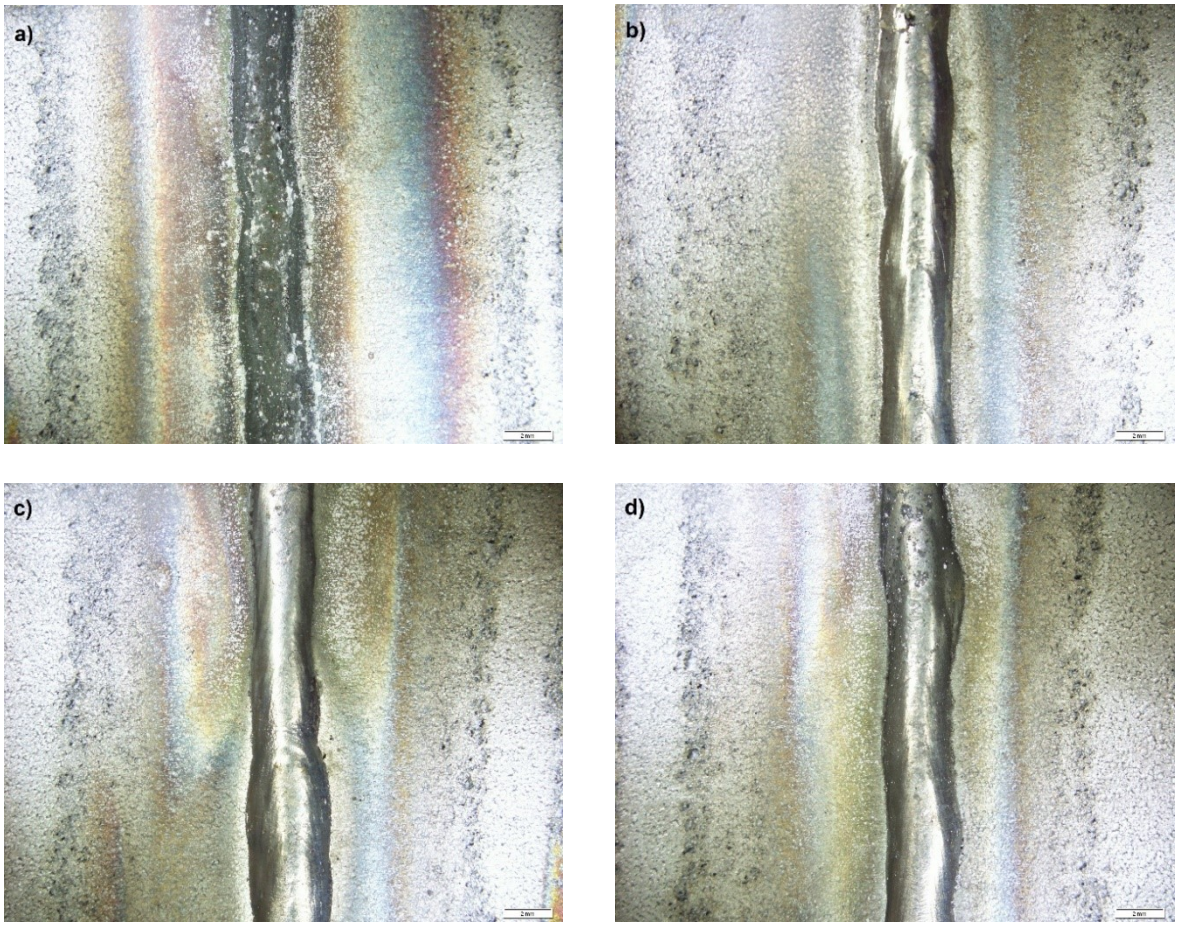

Fig. 44 2101 root weld after 72 hours for: a) no backing gas, b) 100% Ar, c) 100% N_2, d) 95% N_2 + 5% H_2

Results obtained with the LDX 2404 (Tab 14) were inconsistent. An increase in the mass reduction was observed in samples welded with the three different backing gases, compared to the no backing gas sample. A remarkable pitting corrosion was observed at an exact distance from all the welds, with some kind of corrosion product that appeared in the metal surface (Fig.46). The SEM analysis of this detrimental phase transformation is a part of a future work.

Table 14 Corrosion test results for LDX 2404

Backing gas	Original mass (g)	Mass after 72h (g)	Mass reduction after 72h (%)	Corrosion rate (g/cm2)
No gas	18,49	17,73	4,11	0,04
100% Ar	19,32	18,44	4,55	0,04
100% N_2	19,65	18,72	4,73	0,05
95% N_2 + 5% H_2	17,66	16,89	4,36	0,04

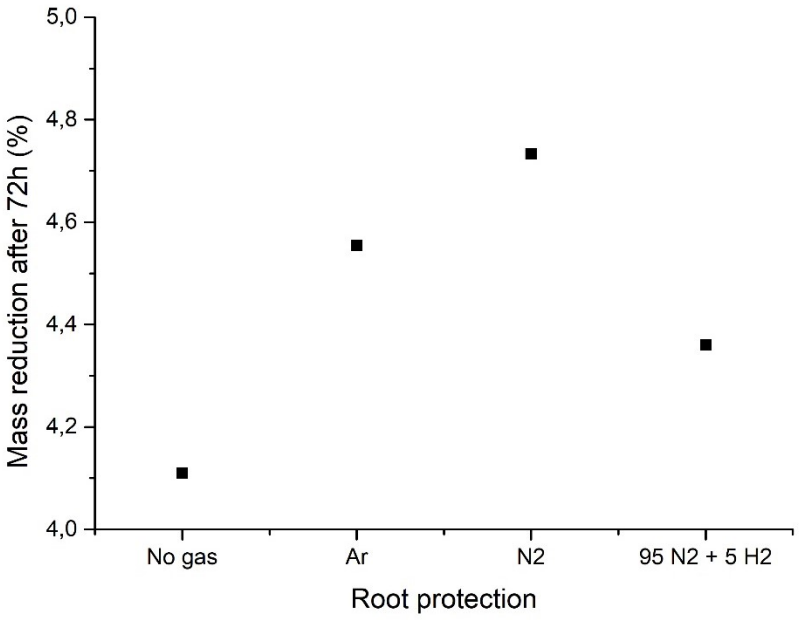

Fig. 45 Values of LDX 2404 mass reduction after 72h (%) relating to the different backing gases

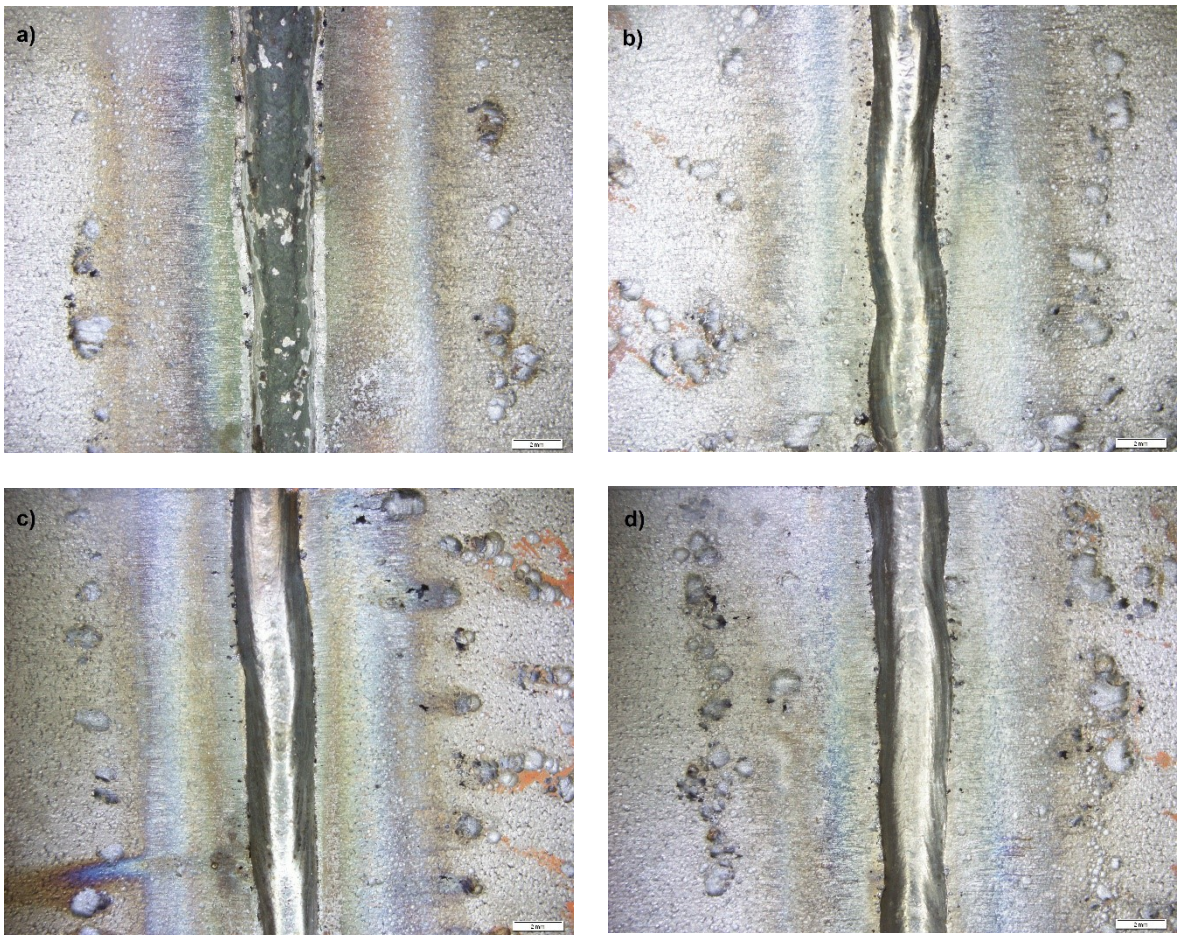

Fig. 46 2404 root weld after 72 hours for: a) no backing gas, b) 100% Ar, c) 100% N_2, d) 95% N_2 + 5% H_2

As explained in the procedure chapter 4.2, the corrosion resistance evaluation made in this work was based only on the weight loss measure. For this reason, because of the slight variations of mass measured during the test, it can give only qualitative indication about corrosion rate. For a reliable quantitative measurement of corrosion resistance, polarization techniques and CPT measurements must be used, in order to obtain detailed information on active/passive behaviour and different critical pitting temperatures. These tests are planned in a running project.

CONCLUSIONS

Duplex stainless steels (UNS S32750, UNS S32101 and UNS S82441) have been investigated in this work, with the purpose of studying the main microstructural transformations these materials may suffer if they undergo heat treatments or welding processes. The investigation has been conducted focusing on the effects that these microstructural transformations have on corrosion resistance and mechanical properties of the selected materials. The following conclusions allow for a better comprehension of the application limits of these particular materials, whose application interest is constantly increasing.

In the first experiment, the decomposition kinetics of ferritic phase (α) in isothermally aged UNS S32750 (SAF 2507) super duplex stainless steel has been investigated for T=800°C and T=850°C. The eutectic decomposition of ferrite into σ-phase and secondary austenite has been clearly observed with OM analysis, for both aging temperatures. T=850°C has been found to be the most critical one, with precipitates of σ-phase visible on the ferrite/austenite junction already after 5 minutes. The amount of σ-phase increased at the expense of the ferritic phase with increasing aging times. For T=800°C the decomposition process followed the same mechanism, but it was significantly slower, with an incubation time of 30 minutes.
Magnetic tests have been employed to quantify the amount of ferromagnetic phase in the different samples. Results showed the tendency of ferrite to decrease with increasing aging times. For both aging temperatures, the experimental data related to the σ-phase precipitation showed to be in accordance with the JMA model. The results of Vickers hardness test showed that hardness of the samples significantly increased with increasing aging time. From a starting value of 260 HV, a maximum value of 370HV has been measured after 45 minutes at T=850°C. This results proved that the eutectic decomposition of ferrite yields remarkable hardening and embrittlement of the parent material, due to the increase of σ-phase content generated by the transformation.

In the second experiment, the effects of Nd: YAG laser welding on microstructure and mechanical/corrosion properties of UNS S32750 (SAF 2507) SDSS samples with different grades of deformation (i.e. ε=0%,10%,20%,30%,40%,50%,60%) have been examined. In all the joints, a strongly unbalanced microstructure mostly consisting of ferritic phase has been observed. The ferrite grains formed as massive particles, with a low percentage of austenite phase precipitated both at ferrite grain boundaries and within the grains. The tendency of the ferrite content to decrease with increasing distances from the middle of the joint has been observed.
Because of the high cooling rate of the laser beam welding process, the HAZ was almost undetectable and no defects or precipitations have been observed. All the

results highlighted that previously cold rolled deformations had no effects either on the microstructure of HAZ/WZ or on the mechanical/corrosion properties of the samples. The Vickers microhardness test conducted in all the joints showed that the unbalanced ferritic structure caused an increase in the hardness values of WZ and HAZ compared to the base metal. Lastly, a constant corrosion rate was observed in the weld zone of all the samples due to the unbalanced austenite/ferrite ratio. The joints have been found highly damaged, and pitting holes could be observed by the naked eye. Quantitative measurement of corrosion resistance as polarization techniques and CPT measurements are planned in a running project

As a final study, the effect of backing gas composition (100% Ar, 100% N2 and 95% N2+5 % H2) on the microstructure and corrosion properties of UNS S32101 (LDX 2101) and UNS S82441 (LDX 2404) have been investigated.
For both materials, microstructure analysis showed that the use of nitrogen-containing backing gases produced a slight increase in austenite content compared to the 100% argon and no-baking gas configurations. The austenitic phase precipitated as both grain boundary allotriomorphic austenite and Widmanstätten side plates. The increase in austenite content should bring to a better corrosion resistance. The corrosion test (72h of immersion in a ferric chloride solution at T= 50 ± 2°C) showed different behaviours in the two materials. For LDX 2101, the presence of nitrogen in the baking gas brought to a slight decrease in mass reduction compared to the samples welded with full argon and no backing gas, in according with the increase of austenite observed in the microstructure. For LDX 2404 the opposite tendency was observed. We can conclude that the corrosion resistance evaluation based only on the weight loss measure was not suitable for this experiment. For a reliable quantitative measurement of corrosion resistance, polarization techniques and CPT measurements must be used, in order to obtain detailed information on active/passive behaviour and different critical pitting temperatures. These tests are planned in a running project.

BIBLIOGRAFY

[1] R. N. Gunn, Ed., Duplex stainless steels: microstructure, properties and applications ; [based ... on the keynote papers from the Glasgow and Beaune conferences]. Cambridge: Abington, 1997.

[2] I. Alvarez-Armas and S. Degallaix-Moreuil, Eds., Duplex stainless steels. London : Hoboken, NJ: ISTE ; J. Wiley, 2009.

[3] J. O. Nilsson, “Super duplex stainless steels,” Mater. Sci. Technol., vol. 8, pp. 685–700, 1992.

[4] M. Breda, “Phase stability in Duplex Stainless Steels,” Phd work, 2014.

[5] M. Bianchi, “Effects of cold rolling on phase precipitation and phase transformation in a 2507 SDSS,” Msc work, 2011.

[6] F. Bonollo and A. Tiziani, “Acciai inossidabili innovativi,” Vicenza, 1998.

[7] E. C. Bain and W. E. Griffiths, “An introduction to the iron-chromium-nickel alloys,” Trans AIME, vol. 75, pp. 166–211, 1927.

[8] “French patent, Nouveaux alliages inoxydables, no. 803361, 1936.”

[9] G. Fassina, “Effects of cold rolling on austenite to α ’ martensite transformation in 2101 lean duplex stainless steel,” Msc work, 2010.

[10] D. Pegoraro, “Modificazioni microstrutturali prodotte dalla deformazione plastica nell’acciaio duplex 2507,” Msc work, 2010.

[11] H. Okamoto, “The Effect of Tungsten and Molybdenum on the Performance of Super Duplex Stainless Steels,” Proc Conf Appl. Stainl. Steels ‘92, vol. 1, pp. 360–369, 1992.

[12] A. L. SCHAEFLER, “Constitution diagram for stainless steel,” Met. Prog, vol. 56, pp. 680–688, 1949.

[13] A. Todesco, “Effects of heat treatment and cold rolling on kinetics of ferrite decomposition processes in DSS 2507,” Msc work, 2016.

[14] E. Ramous, “La Metallurgia Italiana,” vol. 4, p. 37, 2004.

[15] B. Sundman, B. Jansson, and J. O. Andersson, “The Thermo-Calc Databank System,” Calphad, vol. 9, pp. 153–190, 1985.

[16] H. D. Solomon and T. Devine, “Duplex Stainless Steels - A table of two phases,” Proc Conf Duplex Stainl. Steels ASM Mater. Park, pp. 693–756, 1984.

[17] J. Charles, “Super duplex stainless steels- Structure and properties,” Proc Conf Duplex Stainl. Steels 91 Ed. Pisique Uli Cedex, pp. 3–48, 1991.

[18] “Muller.” [Online]. Available: http://www.mueller-behaelterbau.de/en/references/tank-farm.html.

[19] I. Mészáros and P. J. Szabó, “Complex magnetic and microstructural investigation of duplex stainless steel,” NDT E Int., vol. 38, no. 7, pp. 517–521, Oct. 2005.

[20] X. Wang, W. Chen, and H. Zheng, “Influence of isothermal aging on σ precipitation in super duplex stainless steel,” Int. J. Miner. Metall. Mater., vol. 17, no. 4, pp. 435–440, Aug. 2010.
[21] M. Ma, H. Ding, R. D. K. Misra, Z. Y. Tang, H. B. Li, and G. W. Fan, “A study on precipitation kinetics of sigma phase in a hot-rolled super duplex stainless steel during isothermal aging based on the Johnson–Mehl–Avrami model,” Ironmak. Steelmak., vol. 44, no. 4, pp. 311–318, Apr. 2017.
[22] N. Llorca-Isern, H. López-Luque, I. López-Jiménez, and M. V. Biezma, “Identification of sigma and chi phases in duplex stainless steels,” Mater. Charact., vol. 112, pp. 20–29, Feb. 2016.
[23] M. K. Mishra, A. G. Rao, R. Sarkar, B. P. Kashyap, and N. Prabhu, “Effect of Preaging Deformation on Aging Characteristics of 2507 Super Duplex Stainless Steel,” J. Mater. Eng. Perform., vol. 25, no. 2, pp. 374–381, Feb. 2016.
[24] T. Berecz, É. Fazakas, I. Mészáros, and I. Sajó, “Decomposition Kinetics of Ferrite in Isothermally Aged SAF 2507-Type Duplex Stainless Steel,” J. Mater. Eng. Perform., vol. 24, no. 12, pp. 4777–4788, Dec. 2015.
[25] E. Bettini, U. Kivisäkk, C. Leygraf, and J. Pan, “Study of Corrosion Behavior of a 2507 Super Duplex Stainless Steel: Influence of Quenched-in and Isothermal Nitrides,” Int. J. Electrochem. Sci., vol. 9, no. 1, pp. 61–80, 2014.
[26] I. Mészáros, “Testing of stainless steel by double yoke DC magnetometer,” J. Electr. Eng., vol. 61, no. 7, pp. 62–65, 2010.
[27] B. D. Cullity and C. D. Graham, Introduction to magnetic materials, 2nd ed. Hoboken, N.J: IEEE/Wiley, 2009.
[28] F. Fiorillo, Measurement and characterization of magnetic materials. Amsterdam: Elsevier, 2004.
[29] “Avrami equation.” [Online]. Available: https://en.wikipedia.org/wiki/Avrami_equation.
[30] M. Bolut, C. Y. Kong, J. Blackburn, K. A. Cashell, and P. R. Hobson, “Yb-fibre Laser Welding of 6 mm Duplex Stainless Steel 2205,” Phys. Procedia, vol. 83, pp. 417–425, 2016.
[31] A.-M. El-Batahgy, A.-F. Khourshid, and T. Sharef, “Effect of Laser Beam Welding Parameters on Microstructure and Properties of Duplex Stainless Steel,” Mater. Sci. Appl., vol. 2, no. 10, pp. 1443–1451, 2011.
[32] S. Saravanan, K. Raghukandan, and N. Sivagurumanikandan, “Pulsed Nd: YAG laser welding and subsequent post-weld heat treatment on super duplex stainless steel,” J. Manuf. Process., vol. 25, pp. 284–289, Jan. 2017.
[33] S. G, S. S, and R. K, “Investigation of microstructure and mechanical properties of Nd:YAG laser welded lean duplex stainless steel joints,” Opt. - Int. J. Light Electron Opt., vol. 131, pp. 1–10, Feb. 2017.
[34] G. R. Mohammed, M. Ishak, S. N. Aqida, and H. A. Abdulhadi, “The effect of fiber laser parameters on microhardness and microstructure of duplex stainless steel,” MATEC Web Conf., vol. 90, p. 1024, 2017.

[35] F. Mirakhorli, F. Malek Ghaini, and M. J. Torkamany, “Development of Weld Metal Microstructures in Pulsed Laser Welding of Duplex Stainless Steel,” J. Mater. Eng. Perform., vol. 21, no. 10, pp. 2173–2176, Oct. 2012.
[36] M. Keskitalo, K. Mäntyjärvi, J. Sundqvist, J. Powell, and A. F. H. Kaplan, “Laser welding of duplex stainless steel with nitrogen as shielding gas,” J. Mater. Process. Technol., vol. 216, pp. 381–384, Feb. 2015.
[37] M. S. F. de Lima, S. M. de Carvalho, V. Teleginski, and M. Pariona, “Mechanical and Corrosion Properties of a Duplex Steel Welded using Micro-Arc or Laser,” Mater. Res., vol. 18, no. 4, pp. 723–731, Aug. 2015.
[38] V. Quiroz, A. Gumenyuk, and M. Rethmeier, “Laser Beam Weldability of High-Manganese Austenitic and Duplex Stainless Steel Sheets,” Weld. World, vol. 56, no. 1–2, pp. 9–20, Jan. 2012.
[39] V. Amigó, V. Bonache, L. Teruel, and A. Vicente, “Mechanical properties of duplex stainless steel laser joints,” Weld. Int., vol. 20, no. 5, pp. 361–366, May 2006.
[40] C. Köse and R. Kaçar, “Mechanical Properties of Laser Welded 2205 Duplex Stainless Steel*,” Mater. Test., vol. 56, no. 10, pp. 779–785, Oct. 2014.
[41] D. J. Kotecki and T. Siewert, “WRC-1992 Constitution Diagram for Stainless Steel Weld Metals: A Modification of the WRC-1988 Diagram,” AWS Annu. Meet., pp. 171–178, 1992.
[42] E. M. Westin, Microstructure and properties of welds in the lean duplex stainless steel LDX 2101. Stockholm: Department of Materials Science and Engineering, Division of Physical Metallurgy, Royal Institute of Technology, 2010.
[43] E. M. Westin, M. M. Johansson, L.-å. Bylund, and R. F. A. Pettersson, “Effect on microstructure and properties of super duplex stainless steel welds when using backing gas containing nitrogen and hydrogen,” Weld. World, vol. 58, no. 3, pp. 347–354, May 2014.
[44] E. M. Westin, M. M. Johansson, and R. F. A. Pettersson, “Effect of nitrogen-containing shielding and backing gas on the pitting corrosion resistance of welded lean duplex stainless steel LDX 2101® (EN 1.4162, UNS S32101),” Weld. World, vol. 57, no. 4, pp. 467–476, Jul. 2013.
[45] E. M. Westin and A. Fellman, “Effect of laser and laser hybrid welding on the corrosion performance of a lean duplex stainless steel,” J. Laser Appl., vol. 22, no. 4, pp. 150–158, Nov. 2010.
[46] E. M. Westin, M. M. Johansson, L.-å. Bylund, and R. F. A. Pettersson, “Effect on microstructure and properties of super duplex stainless steel welds when using backing gas containing nitrogen and hydrogen,” Weld. World, vol. 58, no. 3, pp. 347–354, May 2014.
[47] E. M. Westin, M. M. Johansson, and R. F. A. Pettersson, “Effect of nitrogen-containing shielding and backing gas on the pitting corrosion resistance of welded lean duplex stainless steel LDX 2101® (EN 1.4162, UNS S32101),” Weld. World, vol. 57, no. 4, pp. 467–476, Jul. 2013.
[48] J. Niagaj and ł. Mazur, “Ferrite content measurements in S32101 lean duplex stainless steel and its welded joints,” Arch. Metall. Mater., vol. 57, no. 3, Jan. 2012.